Dalton Transactions

ROYAL SOCIETY OF CHEMISTRY

PAPER

View Article Online
View Journal | View Issue

Cite this: *Dalton Trans.*, 2021, **50**, 7571

Tetrairon(II) extended metal atom chains as single-molecule magnets†

Alessio Nicolini, [a,b] Marco Affronte,[b] Daniel J. SantaLucia, [c] Marco Borsari, [a] Benjamin Cahier,[d] Matteo Caleffi, [b] Antonio Ranieri, [e] John F. Berry [c] and Andrea Cornia *[a]

Received 26th March 2021,
Accepted 3rd May 2021

DOI: 10.1039/d1dt01007g

rsc.li/dalton

Iron-based extended metal atom chains (EMACs) are potentially high-spin molecules with axial magnetic anisotropy and thus candidate single-molecule magnets (SMMs). We herein compare the tetrairon(II), halide-capped complexes $[Fe_4(tpda)_3Cl_2]$ (**1Cl**) and $[Fe_4(tpda)_3Br_2]$ (**1Br**), obtained by reacting iron(II) dihalides with $[Fe_2(Mes)_4]$ and N^2,N^6-di(pyridin-2-yl)pyridine-2,6-diamine (H_2tpda) in toluene, under strictly anhydrous and anaerobic conditions (HMes = mesitylene). Detailed structural, electrochemical and Mössbauer data are presented along with direct-current (DC) and alternating-current (AC) magnetic characterizations. DC measurements revealed similar static magnetic properties for the two derivatives, with $\chi_M T$ at room temperature above that for independent spin carriers, but much lower at low temperature. The electronic structure of the iron(II) ions in each derivative was explored by *ab initio* (CASSCF-NEVPT2-SO) calculations, which showed that the main magnetic axis of all metals is directed close to the axis of the chain. The outer metals, Fe1 and Fe4, have an easy-axis magnetic anisotropy (D = –11 to –19 cm^{-1}, $|E/D|$ = 0.05–0.18), while the internal metals, Fe2 and Fe3, possess weaker hard-axis anisotropy (D = 8–10 cm^{-1}, $|E/D|$ = 0.06–0.21). These single-ion parameters were held constant in the fitting of DC magnetic data, which revealed ferromagnetic Fe1–Fe2 and Fe3–Fe4 interactions and antiferromagnetic Fe2–Fe3 coupling. The competition between super-exchange interactions and the large, noncollinear anisotropies at metal sites results in a weakly magnetic non-Kramers doublet ground state. This explains the SMM behavior displayed by both derivatives in the AC susceptibility data, with slow magnetic relaxation in **1Br** being observable even in zero static field.

Introduction

An extended metal atom chain (EMAC) is a 1D array of at least three metal (M) ions supported by polydentate organic ligands, which are often helically wrapped around the metal chain.[1–4] They can be homo- or heterometallic, homovalent or mixed-valent species.[3,5] Oligo-α-pyridylamines or related proligands, like dipyridin-2-yl-amine (Hdpa) and N^2,N^6-di(pyridin-2-yl)pyridine-2,6-diamine (H_2tpda),[6,7] are widely used in this research area and are shown in Scheme 1. Their geometry and multidentate nature enforce close distances between the metal centers allowing for the formation of M–M bonds and/or strong magnetic interactions.[1,5] Due to their structural and electronic properties, EMACs have been examined as possible wires in molecular electronics.[5,8–11] They also attracted interest as molecular magnetic materials after chromium(II)-based Cr_3 and Cr_5 EMACs,[12,13] as well as the Mo_2Cr and W_2Cr heterometallic variants,[14,15] showed single-molecule magnet (SMM) properties in their S = 2 ground state. SMMs are molecular compounds displaying directional bistability of the magnetic moment at low temperature[16,17] and are being currently investigated for forefront applications in spintronics, quantum

[a]*Department of Chemical and Geological Sciences, University of Modena and Reggio Emilia & INSTM, I-41125 Modena, Italy. E-mail: acornia@unimore.it*
[b]*Department of Physics, Informatics and Mathematics, University of Modena and Reggio Emilia, I-41125 Modena, Italy*
[c]*Department of Chemistry, University of Wisconsin-Madison, 1101 University Avenue, Madison, Wisconsin 53706, USA*
[d]*Max-Planck-Institut für Kohlenforschung, Kaiser-Wilhelm-Platz 1, 45470 Mülheim an der Ruhr, Germany*
[e]*Department of Life Sciences, University of Modena and Reggio Emilia, I-41125 Modena, Italy*

†Electronic supplementary information (ESI) available: Mass spectra of **1Br** (Fig. S1–S3), scale-expanded ^{1}H NMR spectrum of **1Br** (Fig. S4), full-range ^{1}H NMR spectrum of H_2tpda (Fig. S5), UV-Vis-NIR spectrum of **1Br** (Fig. S6), single crystal X-ray diffraction details for **1Br**·2.3CH_2Cl_2·Et_2O (supplementary Notes 1 and 2, Tables S1–S3), additional tables (S4 and S5) and figures (S7–S9) on electrochemistry, Mössbauer spectroscopy details (supplementary Note 3, eqn (S1)) and additional fits to the 77 K datasets (Fig. S10 and S11), details on AOM calculations (supplementary Note 4, eqn (S2)–(S8), Tables S6–S8 and Fig. S12), additional tables (S9–S11) on *ab initio* calculations, details on spin Hamiltonian models (supplementary Note 5, Tables S12–S14 and Fig. S13–S17), Zeeman diagrams (Fig. S18 and S19) and local spin components in models m**1Cl**D and m**1Br**D (Fig. S20–S22 and Table S15), additional field-dependent AC magnetic susceptibility data (Fig. S23), $\ln(\chi_M''/\chi_M')$ *vs.* $1/T$ plots (Fig. S24), and best-fit parameters from the extended Debye model (Tables S16 and S17) for **1Br**·2.3CH_2Cl_2·Et_2O. CCDC 2072514. For ESI and crystallographic data in CIF or other electronic format see DOI: 10.1039/d1dt01007g

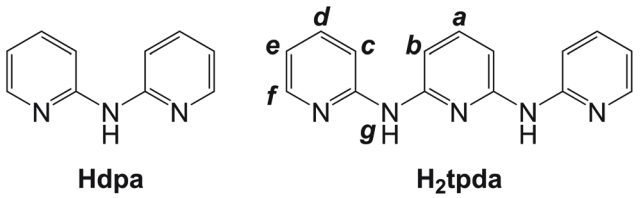

Scheme 1 Structures of the oligo-α-pyridylamine proligands Hdpa and H_2tpda.

technologies,[18–21] and data storage.[22–24] In terms of working temperature, the best-performing SMMs to date are mononuclear complexes of lanthanoids, which can display a memory effect above the boiling temperature of liquid nitrogen (77 K).[25–27] An alternative to the use of lanthanoids is the stabilization of highly magnetic electronic states in polynuclear transition metal compounds, through M–M bonds or ferromagnetic interactions. Especially in the chemistry of Fe and Co it is not uncommon to find compounds with a giant, thermally persistent magnetic moment as a consequence of the direct interaction between d-orbitals.[28,29] In this context, iron(II)-based EMACs have arisen as appealing synthetic targets, because of the large magnetic anisotropy and spin value of high-spin (HS) iron(II).[30,31] Although Fe^{2+} ions were included in some heterometallic EMACs,[5,32–39] homometallic iron(II)-based EMACs proved extremely challenging to synthesize because of the tendency of Fe^{2+} ions to undergo facile oxidation and/or hydrolysis processes. In fact, to the best of our knowledge, only three homometallic iron(II)-based EMACs have been reported so far. In 1998 Cotton *et al.* described the trinuclear complex $[Fe_3(DPyF)_4](PF_6)_2$ (**2**) (HDPyF = *N*,*N*′-di(2-pyridyl)formamidine),[40] in which Fe···Fe separations (2.78 Å) are too large for a metal–metal bond. Nevertheless, the room-temperature effective magnetic moment is not far from the expected value for an S = 6 state, suggesting strongly ferromagnetic interactions. In 2018 we reported the first iron(II)-based EMAC supported by oligo-α-pyridylamido ligands, $[Fe_4(tpda)_3Cl_2]$ (**1Cl**).[41] This chloride-capped complex has idealized three-fold symmetry and a helical structure, and was synthesized by reacting H_2tpda with $[Fe_2(Mes)_4]$ and $Fe_4Cl_8(thf)_6$ in toluene under strictly anhydrous and anaerobic conditions (HMes = mesitylene). It also contains no Fe–Fe bonds but features dominant ferromagnetic interactions at room temperature, although the ground state is only weakly magnetic. In addition, it exhibits SMM behavior only observable in a small static magnetic field (H_{DC}). Very recently, using the silylated Hdpa derivative 2,6-bis[(trimethylsilyl)amino]pyridine (H_2L), Guillet and co-workers were able to isolate $[Fe_3L_3]$ (**3**), the first iron(II)-based EMAC with Fe–Fe bonds (2.44 Å). Its room-temperature effective magnetic moment in benzene hints at a well-isolated S = 6 state.[42]

We have now used the same synthetic technique that allowed to access **1Cl** to prepare its bromo analogue, $[Fe_4(tpda)_3Br_2]$ (**1Br**). We herein present a detailed comparison of the structural, electrochemical, and magnetic properties of the two congeners. In addition, to aid the analysis of direct-current (DC) magnetic data we have investigated the electronic structure of the constituent Fe^{2+} ions by *ab initio* (CASSCF-NEVPT2-SO) methods, considerably improving over our previous analysis of **1Cl** by angular overlap model (AOM) calculations.[41] We have found large single-ion anisotropies, whose competition with super-exchange interactions gives rise to a non-Kramers doublet ground state featuring a noncollinear spin arrangement. This weakly magnetic ground state explains the observation of SMM behavior in alternating-current (AC) magnetic studies conducted on both derivatives, with slow magnetic relaxation of **1Br** being detectable even at H_{DC} = 0.

Experimental section

Materials and methods

All synthetic operations involving iron(II) complexes were carried out inside an MBraun UniLAB glovebox under an inert and controlled dinitrogen atmosphere (H_2O and O_2 < 1 ppm), continuously purified over activated charcoal, molecular sieves, and copper as a dioxygen scavenger. All chemicals were of reagent grade and used as received, unless otherwise noted. Dichloromethane, toluene, acetone and 1,4-dioxane were purchased anhydrous. Tetrahydrofuran and Et_2O were pre-dried over KOH[43] and $CaCl_2$,[44] respectively, and subsequently distilled from their sodium diphenylketyl solutions before use. With the exception of acetone, all solvents (including CD_2Cl_2) were deoxygenated through three freeze–pump–thaw cycles and stored over 4 Å molecular sieves. $[Fe_2(Mes)_4]$ was synthesized from $Fe_4Cl_8(thf)_6$ [45] and MesMgBr in thf/1,4-dioxane.[46,47] H_2tpda was prepared by refluxing 2,6-diaminopyridine, 2-fluoropyridine and LiH in toluene/pyridine, following the high-yield procedure that some of us recently reported.[48] The compound $[Fe_4(tpda)_3Cl_2]\cdot 2.6CH_2Cl_2\cdot 0.84Et_2O$ (**1Cl**·$2.6CH_2Cl_2\cdot 0.84Et_2O$) was prepared as previously described.[41] Tetra-*n*-butylammonium chloride (TBACl) and tetra-*n*-butylammonium bromide (TBABr) were recrystallized twice from acetone/Et_2O, washed with Et_2O and dried under vacuum.[44]

Elemental analysis was performed using a ThermoFisher Scientific Flash 2000 analyzer, following brief exposure of the sample to the air (30–60 s). All other characterization data were collected with strict exclusion of dioxygen and water. Electrospray ionization mass spectrometry (ESI-MS) measurements were conducted on a 6310A Ion Trap LC-MS(n) instrument (Agilent Technologies) by direct infusion of dichloromethane solutions and working in positive ion mode. Matrix-assisted laser desorption/ionization tandem time-of-flight mass spectrometry (MALDI-TOF-MS) measurements were performed at the University of Wisconsin–Madison with a Bruker ULTRAFLEX™ III instrument (equipped with a SmartBeam™ laser) using a powdery sample finely milled with a large excess of pure anthracene and working in positive ion mode. The m/z values in the MALDI-TOF-MS spectrum are expressed by setting the isotopic peak of anthracene ($C_{14}H_{10}$) at m/z =

178.08. The electronic spectrum in dichloromethane solution was recorded up to 2000 nm on a Jasco V-570 double beam UV-Vis-NIR spectrometer, using a quartz cuvette sealed with an airtight Teflon® cap (optical path length l = 0.1 cm). The ^{1}H NMR spectrum was recorded at 298 K in CD_2Cl_2 with a Bruker Avance400 FT-NMR spectrometer (400.13 MHz). The chemical shifts are expressed in ppm downfield from Me_4Si as external standard, by setting the residual ^{1}H signal of CD_2Cl_2 at 5.32 ppm. Spectrum processing and analysis were carried out with TopSpin 4.0.6 software[49] (SI = TD, LB = 1.00 Hz).

Synthesis of $[Fe_4(tpda)_3Br_2]\cdot 2.3CH_2Cl_2\cdot Et_2O$ (1Br·2.3CH_2Cl_2·Et_2O)

Iron(III)-free $FeBr_2(thf)_2$[50,51] was prepared by stirring $FeBr_2$ (19.6 mg, 0.0909 mmol) with a five-fold molar excess of Fe^0 powder in thf at room temperature (5 mL). Excess Fe^0 was removed with a magnet and the solution was evaporated to dryness to give $FeBr_2(thf)_2$ as a very light green solid, which was treated with a dark red solution of $[Fe_2(Mes)_4]$ (105.5 mg, 0.1793 mmol) in toluene (3 mL). A suspension of H_2tpda (94.20 mg, 0.3578 mmol) in toluene (4 mL) was then added dropwise under stirring, yielding a light brown suspension. After 5 min, the reaction mixture was gently heated to reflux for 165 min, whereupon it initially turned orange, then gradually darkened to dark orange-brown. After cooling to room temperature, an orange solid was separated from the dark liquid phase by filtration through a fritted glass funnel (porosity G3 or G4) and extracted with CH_2Cl_2 (2 × 25 mL), to give a red solution (for each extraction, the solid and the solvent were stirred together for 90 min). The solvent was evaporated under vacuum until only ~2 mL remained and an orange precipitate had formed. The suspension was cooled down to −35 °C and the liquid phase was carefully removed using a very narrow bore pipette. The solid was thoroughly dried under vacuum to give **1Br** as an orange powder (50 mg, 48%), from which we measured Mössbauer and MALDI-TOF-MS spectra. For all other characterizations the product was crystallized by slow vapour diffusion of Et_2O (75 mL) into the CH_2Cl_2 extract (50 mL). Dark red prisms were obtained and separated easily by flotation from a powdery residue and from minority crystal phases (see ESI Note 1†) and vacuum-dried to remove lattice solvent (30–35% overall yield). Anal. Calc. for **1Br** ($C_{45}H_{33}Br_2Fe_4N_{15}$): C, 46.3; H, 2.85; N, 18.0. Found: C, 45.9; H, 2.9; N, 18.4. UV-Vis-NIR (4.3×10^{-4} M): $\lambda_{max}(CH_2Cl_2)$/nm = 286 (ε/dm^3 mol^{-1} cm^{-1} 3.81×10^4), 370 (3.38×10^4), 448sh. ^{1}H NMR (CD_2Cl_2, 400.13 MHz): δ_H = 3.53 (6H, s), 8.58 (6H, s), 9.80 (3H, s, H*a*), 62.91 (6H, s), 80.50 (6H, s), 119.7 (6H, s). ESI-MS (positive ion mode): m/z = 1030.1 ($[Fe_3(tpda)_3Br]^+$, 100%); 986.1 ($[Fe_3(tpda)_3Cl]^+$, 25). MALDI-TOF-MS (positive ion mode): m/z = 952.2 ($[Fe_3(tpda)_3 + H]^+$, 100%); 1087.3 ($[Fe_4(tpda)_3Br + H]^+$, 9); 1031.3 ($[Fe_3(tpda)_3Br + H]^+$, 2); 1043.3 ($[Fe_4(tpda)_3Cl + H]^+$, 1).

X-ray crystallography of 1Br·2.3CH_2Cl_2·Et_2O

A prismatic crystal of the compound was removed from the mother liquor under nitrogen, rapidly cooled down in a cold dinitrogen stream, and mounted on a Bruker-Nonius X8APEX diffractometer equipped with Mo-$K\alpha$ generator, area detector, and Kryoflex liquid dinitrogen cryostat for data collection at 115(2) K. Acquisition of matrix frames and data collection were carried out using APEX2 software[52] while data reduction used SAINT program.[52] Multi-scan absorption correction was applied with SADABS.[52] Programs SIR92[53] and SHELXL-2014/7,[54] both implemented in the WINGX v2014.1 suite,[55] were used for structure solution and refinement on F_o^2, respectively. Although the molecule has no crystallographically-imposed symmetry, two $tpda^{2-}$ ligands (those containing N7 and N8) are almost perfectly related by a twofold axis normal to the metal chain. The third $tpda^{2-}$ ligand, the metal ions and the terminal bromido ligands lift such local symmetry and are disordered over two unequally populated positions (0.88 : 0.12) related by a 180° rotation around the above-mentioned dyad. As a consequence of this, the minority component is structurally similar to its majority counterpart. All attempts to model the terminal ligands as mixed Br/Cl scatterers with complementary occupancies gave unphysically low (<0.01 Å^2) displacement parameters for the minority (Cl) components. Lattice solvent molecules (CH_2Cl_2 and Et_2O) also show severe positional disorder, with shared occupation of crystallographic sites, which makes their modelling extremely challenging. Non-hydrogen atoms were refined anisotropically, but isotropic displacement parameters had to be used for most disordered portions of the structure. These were refined with further restraints/constraints on geometry and displacement parameters. In particular, similarity restraints were applied to the geometry of CH_2Cl_2 molecules, whereas Et_2O molecules were restrained to the geometry found in CCDC 973959. Hydrogen atoms were treated isotropically and refined using a riding model with $U(H) = 1.2U_{eq}(C)$ for methylene and $U(H) = 1.5U_{eq}(C)$ for methyl hydrogens, which were set in a staggered conformation. Crystal data and refinement parameters are gathered in Table S1† while an exhaustive listing of interatomic distances and angles as well as further details on structural analysis are available in Table S2 and in ESI Note 2.†

Electrochemistry

Cyclic voltammetry (CV) measurements were carried out using a PARSTAT model 2273 potentiostat-galvanostat. Experiments were performed at different scan rates (0.02–5 V s^{-1}) using a cell for small volume samples (0.5 mL). A 1 mm diameter glassy carbon (GC) disk, a Pt wire, and an Ag wire were used as working, counter, and quasi-reference (Ag/AgCl or Ag/AgBr) electrodes, respectively. The GC electrode was cleaned following a previously reported procedure.[41,56] For all the experiments, the potential of the quasi-reference electrode was calibrated against the ferrocenium/ferrocene redox couple (in dichloromethane, E° = 0.460 V *vs.* KCl saturated calomel electrode, SCE).[57] All the reported potential values $E^{\circ\prime}$ are referenced to the ferrocenium/ferrocene redox couple. The formal potential value ($E^{\circ\prime}$) corresponding to each electron transfer (ET) process was calculated as the semi-sum of the cathodic and anodic peak potentials, $E^{\circ\prime} = (E_{pc} + E_{pa})/2$. The dependence of $\Delta E_p = E_{pa} - E_{pc}$ on scan rate yielded the standard hetero-

geneous ET rate constant (k_{ET}),[58] which is the ET rate constant measured at the formal potential $E^{\circ\prime}$. Due to the instability of **1Cl** and **1Br** in the presence of O_2 or H_2O, the experiments were performed in the above-described MBraun UniLAB glovebox at temperatures ranging between −15 and +5 °C.[41] Variable temperature experiments were conducted using an isothermal cell configuration, in which the temperature of the reference and working electrodes was varied. For this experimental configuration, the reduction entropy referenced to the ferrocenium/ferrocene redox couple ($\Delta S^{\circ\prime}_{rc}$) is given by:

$$\Delta S^{\circ\prime}_{rc} = S^{\circ\prime}_{red} - S^{\circ\prime}_{ox} = nF\left(\frac{\partial E^{\circ\prime}}{\partial T}\right)_P \quad (1)$$

Thus, $\Delta S^{\circ\prime}_{rc}$ can be calculated from the slope of the $E^{\circ\prime}$ *vs.* T plot, which is linear under the assumption that $\Delta S^{\circ\prime}_{rc}$ is constant over the limited temperature range investigated. With the same assumption, the enthalpy change (also referenced to the ferrocenium/ferrocene redox couple, $\Delta H^{\circ\prime}_{rc}$) was obtained from the Gibbs–Helmholtz equation, namely as the negative slope of the $E^{\circ\prime}/T$ *vs.* $1/T$ plot. All measurements were made on ~0.2 mM solutions of **1Cl** and **1Br** prepared by dissolving vacuum-dried crystals in CH_2Cl_2 and using 0.1 M TBACl and TBABr, respectively, as supporting electrolytes. The ohmic drop between the working and the reference electrodes was minimized through a careful feedback correction. The experiments were repeated at least five times; $E^{\circ\prime}$ and k_{ET} values were found to be reproducible within ±0.002 V and ±6%, respectively.

Magnetic measurements

Magnetic measurements were made on a Quantum Design PPM cryogenic system with a two-coil susceptometer. A polycrystalline sample of **1Br**·2.3CH_2Cl_2·Et_2O (20.41 mg) and a small amount of its mother liquor (24.08 mg, CH_2Cl_2 : Et_2O 54 : 46) were introduced into a quartz tube, which was subsequently flame-sealed. The presence of the mother liquor was necessary to prevent field-induced torquing at low temperature. The diamagnetic contributions of the sample and of the mother liquor were evaluated using Pascal's constants.[59] The magnetic response of an identical quartz tube was previously measured to correct for the diamagnetic contributions of the quartz.[41] DC measurements were based on the extraction magnetometry technique. Magnetic susceptibility was obtained as $\chi = M/H$ from magnetization (M) measurements in a static magnetic field H = 10 kOe from 300.0 to 2.0 K. The isothermal field dependence of M was also measured at 2, 4, and 8 K, scanning the field up to 70 kOe. AC measurements were performed using a small oscillating magnetic field of 10 Oe (for frequencies ν between 21 and 1715 Hz) or 5 Oe (for ν between 2664 and 9980 Hz) to minimize self-heating of the sample. The influence of H_{DC} on the out-of-phase component of the magnetic susceptibility (χ'') was explored with preliminary χ'' *vs.* ν scans at 2 K for H_{DC} values ranging from 0 to 2.5 kOe. Afterwards, χ'' *vs.* ν scans between 2.0 and 8.0 K were carried out for H_{DC} = 0, 1, and 2 kOe.

Mössbauer spectroscopy

Mössbauer spectra of **1Cl** and **1Br** encased in an eicosane matrix were collected at 10 and 77 K with a 1024 channel See Co model W304 resonant gamma-ray spectrometer using ^{57}Co on Rh foil as a gamma-ray source (initial strength = 25 mCi, obtained from Ritverc Isotope Products) at the University of Wisconsin–Madison. The source velocity range used was ±4 mm s^{-1} and measurements were conducted under vacuum. Cryogenic temperatures were achieved using a Lakeshore model 336 temperature controller in conjunction with a Janis model SHI-850 cryostat. Mössbauer data were fitted with the WMOSS4F software package,[60] using an adaptive nonlinear least-squares algorithm developed by Dennis *et al.* (see ESI Note 3† for further details).[61] Refined parameters for each quadrupole doublet were the isomer shift (δ), the quadrupole splitting (ΔE_Q), and the linewidth, calculated as full-width at half-maximum (FWHM). Errors associated with δ, ΔE_Q, and FWHM are estimated to be ~0.01 mm s^{-1}. All reported isomer shifts are referenced to α-Fe foil at room temperature (294 K). At both temperatures the spectra could be satisfactorily fitted using two doublets with fixed 1 : 1 relative areas (sub-spectra 1 and 2). Attempts to fit more quadrupole doublets to the data did not lead to convergence due to overparameterization. Alternative fits to the 77 K spectra are included in the ESI (Fig. S10 and S11†); while numerically sound, these alternative parameter sets are less consistent with those extracted from the 10 K spectra, which could only be modeled with the parameters reported in Table 3.

AOM calculations

The electronic structure of the iron(II) centers in **1Br** was studied using AOM calculations, carried out with the program package AOMX.[62] Following the same approach developed for the chloro derivative **1Cl**,[41] the X-ray coordinates of Fe1(N1,N2, N3,Br1) and Fe4(N13,N14,N15,Br2) were averaged to C_{3v} symmetry. As for Fe2(N4,N5,N6,N7,N8) and Fe3(N8,N9,N10,N11, N12), the X-ray coordinates were directly used in the calculations. The ligand field (LF) parameters accounting for σ and π interactions[63] were obtained from the values reported for *trans*-[Fe(py)$_4$Br$_2$] and *trans*-[Fe(py)$_4$(NCS)$_2$] (py = pyridine), assuming an r^{-6} dependence on metal–ligand distance r and treating all the N-donor atoms as pyridine-type donors for simplicity.[64–66] Racah parameters for the interelectronic repulsion were fixed at B = 850 cm^{-1} and C = 3100 cm^{-1}, hence ~20% lower than the free ion values.[67] The effective one-electron spin–orbit (SO) coupling constant was fixed at ζ_{3d} = 350 cm^{-1}, while the orbital reduction factor (k) was taken as isotropic and unitary.[66] Further details can be found in ESI Note 4.†

Ab initio calculations

All calculations have been done with the Orca 4.2 package.[68] To extract the local anisotropy of the i-th Fe center, the remaining iron(II) ions were replaced by diamagnetic zinc(II) ions. The zero-field splitting (ZFS) D_i and E_i parameters were evaluated following the procedure developed in ref. 69. A state- averaged

CASSCF (complete active space self-consistent field) calculation was performed; dynamical correlation was taken into account with the domain-based local pair natural orbital 2nd-order N-electron valence state perturbation theory (DLPNO-NEVPT2) method.[70–72] Finally, SO coupling was accounted for by quasi-degenerate perturbation theory with the spin–orbit mean-field (SOMF) Hamiltonian.[73] The complete active space (CAS) is composed of the five mainly-3d orbitals of the Fe centers and the six associated electrons, *i.e.* CAS(6,5). Averaging of the molecular orbitals (MOs) was done over all five quintet and 45 triplet spin states generated by the CAS(6,5)SCF optimization. The SO coupling was considered between all M_S components of these spin states, the spin-free energy (diagonal elements of the SO matrix) being evaluated at the DLPNO-NEVPT2 level. In CASSCF, NEVPT2, and SO calculations, the relativistic Karlsruhe basis sets using a Douglas–Kroll–Hess (DKH) Hamiltonian were used (DKH-def2-TZVP for Fe atoms, DKH-def2-TZVP(-f) for bonding N, Br and Cl atoms and for first neighbor Zn atoms, and DKH-def2-SVP for H atoms).[74] The corresponding def2/JK auxiliary basis was used.[75] Preliminary calculations on various truncated complexes have shown little influence of the truncation on both electronic structure and magnetic properties of the Fe centers. We nevertheless considered the complete structure to avoid any bias.

The principal directions of $\bar{\bar{D}}_i$ and $\bar{\bar{g}}_i$ tensors do not in general coincide.[76] However, the $\bar{\bar{D}}_i$ tensors of three over four metal centers in both **1Cl** and **1Br** have their easy, intermediate, and hard principal axes at small angles from the corresponding principal directions of $\bar{\bar{g}}_i$, *i.e.* the easy direction of $\bar{\bar{D}}_i$ is close to the easy direction of $\bar{\bar{g}}_i$, *etc.* (Table S11†). For Fe1 and Fe2, misalignments in **1Cl** (**1Br**) are in the range 0.58–7.29° (0.38–6.45°). For Fe4 the misalignment is larger, with angles ranging from 4.07 to 20.84° (3.79 to 11.43°). For Fe3, the hard directions of $\bar{\bar{D}}_i$ and $\bar{\bar{g}}_i$ are both approximately along the metal chain (Z), but the two remaining principal axes are strongly misaligned, with offsets close to 45°. This behavior is probably related to the very small rhombic anisotropy of Fe3.

Spin Hamiltonian calculations

The fitting of magnetic data utilized PHI v3.1.5 software.[77] Since PHI allows only one set of Euler angles to be defined for each spin center, the orientation of the $\bar{\bar{g}}_i$ tensor was assumed to coincide with that of the $\bar{\bar{D}}_i$ tensor for i = 1, 2, and 4, a reasonable approximation considering the data in Table S11.† The $\bar{\bar{g}}_3$ tensor is severely misaligned with respect to $\bar{\bar{D}}_3$ in the XY plane. However, its easy and intermediate components are equal to within 0.025 and were averaged to give an axial $\bar{\bar{g}}_3$ tensor. When susceptibility and magnetization data were simultaneously fitted, the minimized quantity was the total residual R defined as:

$$R = \left[\sum_{p=1}^{n}\left(M_{\mathrm{exp},p} - M_{\mathrm{calc},p}\right)^2\right]\left[\sum_{p=1}^{m}\left(\chi_{\mathrm{exp},p} - \chi_{\mathrm{calc},p}\right)^2\right] \quad (2)$$

where n and m are the number of magnetization (M) and susceptibility (χ) datapoints, respectively, while "exp" and "calc" represent experimental and calculated values, respectively. Refined parameters were isotropic super-exchange coupling constants J_{ij} and a correction for temperature independent paramagnetism (TIP). The TIP correction was introduced to better reproduce high-temperature susceptibility data and compensate for possible systematic errors. For each model, the variable space was surveyed prior to the fit, in order to exclude the presence of additional minima in the R hypersurface. Models with anisotropic super-exchange interactions were also tested but did not improve the fit quality. Although magnetic measurements were performed on uncrushed polycrystalline samples restrained in the frozen mother liquor, the crystals were considered small enough to give rise to a powder average. Therefore, calculated susceptibility and magnetization data were integrated over 377 and 233 different directions, respectively, following the Zaremba–Conroy–Wolfsberg scheme as presented by Levitt (Field Powder 6 and 5 in PHI v3.1.5).[77,78] Local spin components were computed using in-house developed software based on ZHEEV routine for matrix diagonalization.[79]

Results and discussion

Synthesis and solution studies

Compound **1Br** was synthesized by a procedure similar to that reported for its chloro analogue **1Cl**.[41] Refluxing $FeBr_2(thf)_2$, $[Fe_2(Mes)_4]$, and H_2tpda in 1 : 2 : 4 molar proportions in toluene under strictly anaerobic and anhydrous conditions gives an orange precipitate. This solid is likely to contain the tetrairon(II) EMAC (Scheme 2), which is only sparingly soluble in toluene but highly soluble in CH_2Cl_2. In fact, extraction of the solid with CH_2Cl_2 gives a red solution whose ESI-MS spectrum is similar to that recorded on a solution of pure **1Br** (*vide infra*). Concentration and cooling of these CH_2Cl_2 extracts affords crude **1Br** in moderate yield as an orange powder. MALDI-TOF-MS (positive ion mode) shows one strong peak at m/z = 952.2 and a much weaker one at m/z = 1087.3, whose isotopic envelopes are consistent with $[Fe_3(tpda)_3 + H]^+$ and $[Fe_4(tpda)_3Br + H]^+$, respectively (Fig. S1†). In addition, two weak signals are also present at m/z = 1031.3 and 1043.3, which are assigned to $[Fe_3(tpda)_3Br + H]^+$ and $[Fe_4(tpda)_3Cl + H]^+$, respectively (Fig. S2†). Traces of chloride salts may be present as contaminants in the $[Fe_2(Mes)_4]$ reactant, but the CH_2Cl_2 solvent may also represent a source of chloride ions during workup. This crude product can be recrystallized by vapour diffusion of Et_2O in a CH_2Cl_2 solution to give **1Br**·2.3CH_2Cl_2·Et_2O as large dark red prisms.

These results confirm that iron amides are accessible *via* $[Fe_2(Mes)_4]$,[80] which performs a dual role in the reaction. It not only acts as a source of iron(II) ions, but also serves as a strong base for deprotonation of H_2tpda, giving an inert hydrocarbon (HMes) as the only by-product. Because of their higher solubility in organic solvents compared to FeX_2, the thf adducts of iron(II) halides are used as additional sources of iron(II) and of the axial halide ligands. In spite of the favourable molar ratios

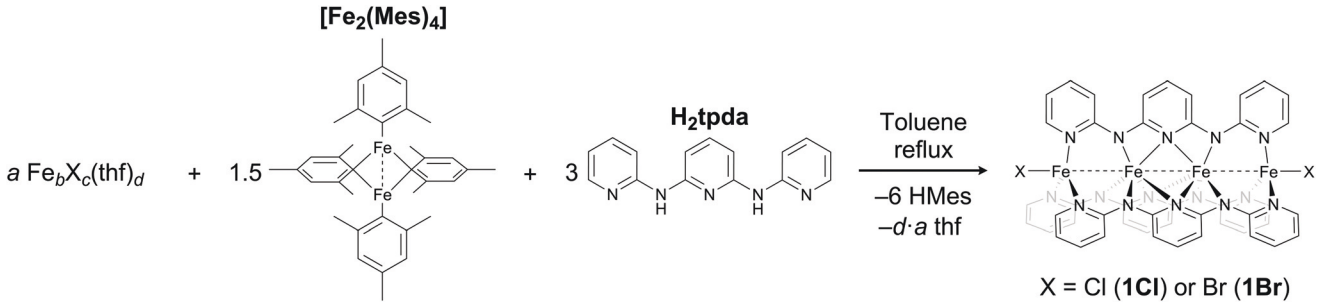

Scheme 2 Synthesis of tetrairon(II) EMACs $[Fe_4(tpda)_3X_2]$, where X = Cl (*a* = 1/4, *b* = 4, *c* = 8, *d* = 6) or Br (*a* = *b* = 1, *c* = *d* = 2).

of the reactants, $[Fe_5(tpda)_4Br_2]$ was not observed or isolated in these experimental conditions.

The ESI-MS spectrum of **1Br** in CH_2Cl_2 (positive ion mode) shows no molecular parent ion peak (Fig. S3†). Instead, two well resolved signals are present at m/z = 1030.1 (100%) and 986.1 (25%), whose isotopic patterns are consistent with the ionic species $[Fe_3(tpda)_3Br]^+$ and $[Fe_3(tpda)_3Cl]^+$, respectively. The same peaks are detected in the ESI-MS spectrum of chloro derivative **1Cl**, but with reversed relative intensity (13 : 100).[41] While formation of $[Fe_3(tpda)_3Br]^+$ in electrosprayed solutions of **1Cl** can only be explained assuming that traces of bromide ions remain from the synthesis of $[Fe_2(Mes)_4]$, the origin of $[Fe_3(tpda)_3Cl]^+$ peak in the spectra of the bromo derivative is less clear. Chloride traces are already present in crude **1Br**, as shown by its MALDI-TOF-MS spectra (see above), but might also be generated by chloride abstraction from CH_2Cl_2 under ESI-MS ionization conditions, as found for other chlorinated solvents.[81,82]

The room-temperature ^{1}H NMR spectrum of **1Br** in CD_2Cl_2 is displayed in Fig. 1 along with that of **1Cl** for comparison. In the two compounds, six paramagnetically shifted singlets (labelled from I to VI) are spread over a range of ~120 ppm with integrated areas in a 2 : 1 : 2 : 2 : 2 : 2 ratio (peak I in **1Br** partially overlaps with the CH_2 quartet of residual Et_2O). All signals except one (I) undergo downfield shifts compared to the signals of the free ligand in CD_2Cl_2 (Fig. S5†). The three lowest-field signals (IV, V and VI) are approximately in the same position in the two compounds. However, significant differences occur in the high-field portion of the spectrum, since the half-intensity resonance (II) is the second highest-field signal in **1Cl** but the third in **1Br**. This is a consequence of the fact that signals I and III are shifted upfield by 2.2–2.4 ppm in **1Br** *vs.* **1Cl**. In both compounds, the observed spectra indicate that – in solution and over the NMR time scale – the molecules adopt the highest possible symmetry for a helical structure (D_3), implying three equivalent $tpda^{2-}$ ligands with C_2 symmetry and six chemically inequivalent H atoms. A similar behavior is displayed by pentachromium(II) EMAC $[Cr_5(tpda)_4Cl_2]$, which exhibits its maximum possible symmetry (D_4) in dichloromethane solution over the NMR time scale, while it is much less symmetric in the solid state.[48] The half-intensity signal II can be firmly assigned to the *p*-H atom of the central pyridine ring (H*a* in Scheme 1). Among the

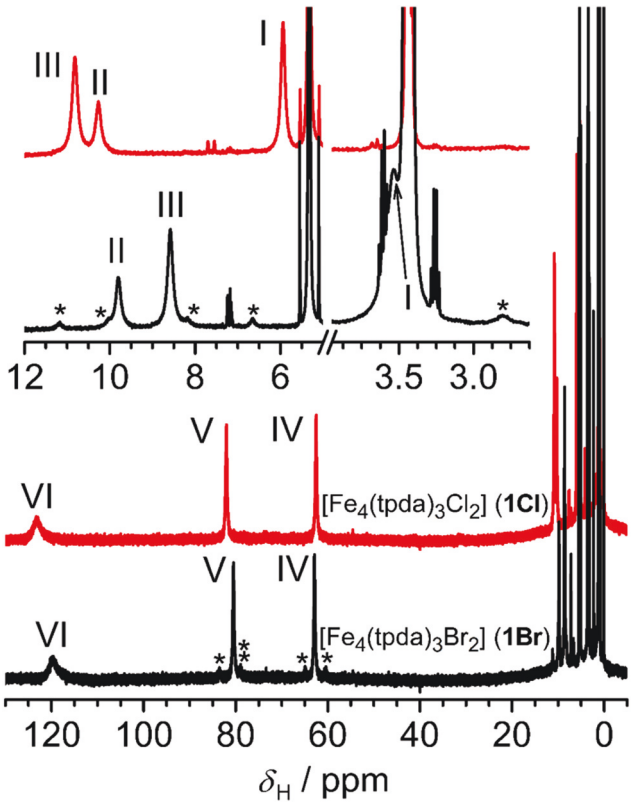

Fig. 1 ^{1}H NMR spectra of **1Cl** (red line) and **1Br** (black line) in CD_2Cl_2 (298 K, 400.13 MHz). Signals of **1Cl** are labelled from I to VI in order of decreasing field; the same scheme is used for **1Br**, except that II still labels the half-intensity signal corresponding to H*a*. The inset shows a magnification of the spectra between 12.0 and 2.6 ppm (no peaks are present between 5.0 and 3.8 ppm). Processing parameters (TopSpin 4.0.6[49]): SI = TD, LB = 1.00 Hz. δ_H (ppm) = 3.43 (Et_2O, CH_2, q, ^3J = 7 Hz), 5.32 (residual protons in CD_2Cl_2), 7.15 (toluene, CH(2,4,6), m), 7.24 (toluene, CH(3,5), m). The spectral region between 2.6 and 0 ppm features no peaks from the compound (Fig. S4†). The spectrum of **1Cl** is taken from ref. 41.

remaining signals, the most downfield-shifted one (VI) is presumably due to *o*-H atoms (H*f*), which lie closest to the terminal iron(II) ions (Fe···H*f* = 2.98–3.16 Å in **1Br** and 2.97–3.13 Å in **1Cl**). Though selective gradient-enhanced 1D-TOCSY on **1Cl** exhibited no signal, a 2D-TOCSY experiment without gradients

evidenced only a very weak cross peak between singlets I and III, which likely arise from the terminal pyridyl groups (H*c–e*). Isotopic-labelling experiments[48] would be required for a complete assignment of the spectrum.

It is important to note that neither the six peaks of **1Br** nor the set of eleven signals expected for a C_3-symmetric hetero-dihalide derivative are detected in the spectrum of **1Cl**. Since the intermolecular exchange of axial ligands is likely to be slow over the NMR timescale,[83] ^{1}H NMR data indicate that the species with axial bromido ligands found in the ESI-MS spectra of **1Cl** are trace impurities undetectable by NMR. However, the spectrum of **1Br** contains an additional set of ten weak singlets with roughly equal intensities, marked with asterisks in Fig. 1. Considering that one signal may be broadened beyond detection or hidden, we tentatively ascribe this pattern to the hetero-dihalide species $[Fe_4(tpda)_3ClBr]$ (**1ClBr**), which is the likely source of chloro complexes found in ESI-MS and MALDI-TOF-MS spectra of **1Br** (see above). Hetero-dihalide tricobalt(II) EMACs were reported by Clérac *et al.*, who identified the species $[Co_3(dpa)_4Cl_2]$ (**4Cl**), $[Co_3(dpa)_4ClBr]$ (**4ClBr**), and $[Co_3(dpa)_4Br_2]$ (**4Br**) in ^{1}H NMR spectra and reported a strong tendency of Cl^- impurities to replace Br^- in pure **4Br**.[83] While the D_4-symmetric species **4Cl** and **4Br** give rise to four proton NMR signals, **4ClBr** has C_4 symmetry and eight ^{1}H NMR signals.[83]

With the proposed assignment, the integrated signal intensities indicate a ~8% mole fraction of **1ClBr**, implying a 96 : 4 proportion of Br^- and Cl^- ligands. This low fraction is consistent with the results of the X-ray structure refinement, which provides no evidence for mixed Br/Cl axial ligands in **1Br**·2.3CH_2Cl_2·Et_2O (*vide infra*).

UV-Vis-NIR spectroscopy data were previously reported for the free ligand in tetrahydrofuran solution.[41] The spectra show two intense absorptions bands, which are assigned to $\pi \rightarrow \pi^*$ transitions and are observed at 262 and 336 nm in H_2tpda, and at 320 and 390 nm $tpda^{2-}$ (Fig. S6†).[41] The electronic spectra of **1Cl** and **1Br** in CH_2Cl_2 solution both present two strong $\pi \rightarrow \pi^*$ transitions, with a slightly lower molar absorptivity (ε) in the latter (Fig. S6†). The two peaks are red shifted as compared with those of H_2tpda and appear at 288 and 374 nm in **1Cl** and at 286 and 370 nm in **1Br**. In addition, they feature a shoulder at 448 nm. The electronic spectra of **1Cl** and **1Br** do not vary over time, but admission of air in the cuvette causes an immediate blueshift of the two main peaks and the disappearance of the shoulder at 448 nm, the final spectrum being superimposable to that of H_2tpda. Interestingly, the single strong band in the UV-Vis spectra of **4Cl** and **4Br** also has a lower ε and a higher energy in the bromo derivative.[83] This behavior can be explained considering the softer character of the bromido ligands, which promote better donation of electron density from the $tpda^{2-}$ molecules and cause a smaller red shift.

X-ray structure

The molecular structure of **1Br**, as determined by single-crystal X-ray diffraction on **1Br**·2.3CH_2Cl_2·Et_2O at 115(2) K, is displayed in Fig. 2. The molecule has no crystallographically imposed symmetry and is partially disordered over two positions with 88 : 12 occupancies; the disorder is only resolvable on one $tpda^{2-}$ ligand, on the four metals, and on the terminal bromido ligands. We herein discuss only the highest-occupancy portion, whose main geometric features are listed in Table 1.

Complex **1Br** is a stringlike species formed by a chain of four metals arranged in a slightly helical zig-zag fashion (Fe···Fe···Fe = 167.7–172.1°, Fe···Fe···Fe···Fe torsion angle =

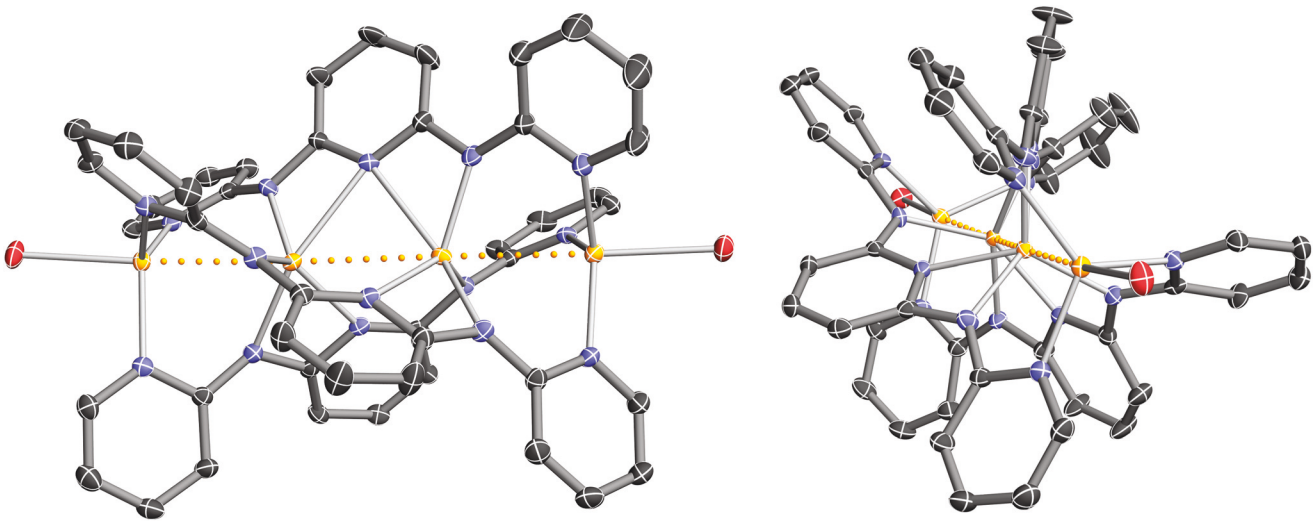

Fig. 2 Molecular structure of **1Br** (right-handed enantiomer), viewed approximately normal to the Br–Fe···Fe···Fe–Br chain (left) and at ~25° from it (right). Color code: orange, Fe; red, Br; blue, N; dark gray, C. Hydrogen atoms and the minority disordered component are omitted for clarity. The dotted lines connecting the Fe centers are a guide to the eye and do not indicate chemical bonds. Thermal ellipsoids are drawn at the 60% probability level.

Table 1 Selected interatomic distances (Å) and angles (°) for **1Br**·2.3CH_2Cl_2·Et_2O

Fe1–Fe2	2.9747(12)
Fe2–Fe3	2.9711(11)
Fe3–Fe4	2.9551(12)
Fe1–Br1	2.5314(11)
Fe4–Br2	2.5100(12)
Fe1–N1	2.089(4)
Fe1–N2	2.067(4)
Fe1–N3	2.096(4)
Fe2–N4	2.108(4)
Fe2–N5	1.993(4)
Fe2–N6	2.011(4)
Fe2–N7	2.175(4)
Fe2–N8	2.492(4)
Fe3–N8	2.500(4)
Fe3–N9	2.234(4)
Fe3–N10	2.042(4)
Fe3–N11	2.036(4)
Fe3–N12	2.087(4)
Fe4–N13	2.088(4)
Fe4–N14	2.088(4)
Fe4–N15	2.071(5)
Br1–Fe1–Fe2	177.01(6)
Fe1–Fe2–Fe3	172.08(4)
Fe2–Fe3–Fe4	167.67(6)
Fe3–Fe4–Br2	178.62(8)

168.1°) and wrapped together by three all-*syn* $tpda^{2-}$ anions (Fig. 2). Each end of the chain is capped by one bromido ligand, with no crystallographic evidence for a detectable fraction of terminal chlorides (see Experimental section). **1Br** is indeed the first $tpda^{2-}$-based EMAC with bromido capping ligands.

Charge neutrality considerations and Bond-Valence Sum (BVS) calculations (Table S3†) demonstrate that all four metal centers are HS iron(II), as confirmed by Mössbauer spectra (*vide infra*). The structure is almost superimposable to that of chloro analogue **1Cl** in **1Cl**·2.6CH_2Cl_2·0.84Et_2O, as shown in Fig. 3. The main difference is represented by the Fe–X (X = Br, Cl) distances, which are about 6% longer for Br (2.510–2.531 Å) *vs.* Cl (2.358–2.386 Å).[41] To the best of our knowledge, no other

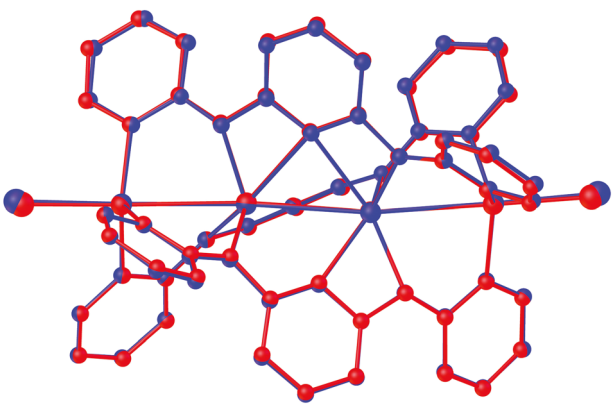

Fig. 3 Superimposed molecular structures of **1Cl** (red) and **1Br** (blue) drawn using a ball-and-stick model (right-handed enantiomers). The minority disordered component in **1Br** and hydrogen atoms in both **1Cl** and **1Br** are omitted for clarity. The lines connecting the Fe centers do not indicate chemical bonds.

EMACs containing $tpda^{2-}$ and different axial halides are known. However, a comparison can be made with trimetallic chains supported by dpa^-, the shorter congener of $tpda^{2-}$ (Scheme 1). The structures of $[M_3(dpa)_4Cl_2]$ and $[M_3(dpa)_4Br_2]$ are reported for M = Cr^{2+} (213 K),[84] Co^{2+} (109–111 K),[83,85] and Cu^{2+} (295 K).[86,87] In these complexes the M–X bond distance also increases by 5–8% when replacing Cl with Br.

The Fe···Fe distances in **1Br** range from 2.955 to 2.975 Å and are hence comparable with those found in **1Cl** (2.941 to 2.991 Å). They are far too large for a metal–metal bond, but shorter than in dpa^- based diiron(II) complexes, such as $[Fe_2(dpa)_2(Mes)_2]$[80] (**5**; 3.104(2) Å), $[Fe_2(dpa)_3Cl]$[80] (**6**; 3.043(1) Å) and $[Fe_2(dpa)_2(hmds)_2]$[88] (**7**; Hhmds = 1,1,1,3,3,3-hexamethyldisilazane; 3.3609(1) Å). Triiron(II) complexes **2** and **3** present considerably shorter Fe···Fe distances of 2.782(1)–2.783(1) and 2.4416(5) Å, respectively, consistent with the presence of metal–metal bonds in the latter.[40,42]

The coordination geometry of the metal centers is highlighted in Fig. 4. The terminal iron centers (Fe1 and Fe4) possess a distorted trigonal-pyramidal coordination environment, afforded by three pyridyl N atoms (N_{py}) and one terminal bromido ligand (Fe–N_{py} = 2.067–2.096 Å, N_{py}–Fe–N_{py} = 110.8–125.7°, Br–Fe–N_{py} = 95.1–98.4°). The internal iron centers (Fe2 and Fe3) are pentacoordinated, with a very distorted geometry. Each of them is primarily involved in three short contacts with amido N atoms (N4, N5, N6 and N10, N11, N12, Fe–N = 1.993–2.108 Å). In addition, Fe2 and Fe3 have a slightly longer contact with the central N_{py} atoms of two different $tpda^{2-}$ ligands (N7 and N9, Fe–N = 2.175–2.234 Å). The central N_{py} atom (N8) of the third $tpda^{2-}$ ligand is involved in a longer coordination bond with both Fe2 and Fe3, thus completing their coordination spheres (Fe–N8 = 2.492–2.500 Å). It is worth noting that only this $tpda^{2-}$ ligand is almost symmetrically bonded to the metal chain (Fe2–N8 ≈ Fe3–N8). The remaining two ligands are asymmetrically positioned, so that in the solid state **1Br** does not achieve the maximum possible symmetry for a helical structure (D_3) but approaches twofold symmetry perpendicular to the metal chain. Each $tpda^{2-}$ ligand is helically wrapped around the linear array of metal ions, due to steric interactions between pyridyl *β*-H atoms (H*b* and H*c* in Scheme 1). As a result of this twisting, the dihedral angle between neighboring pyridine rings of the same $tpda^{2-}$ ligand ranges from 36° to 53° (Fig. 2, on the right). The molecule is thus chiral, but both enantiomers are found in a 1 : 1 ratio in the centrosymmetric crystal structure.

For comparison, the other $tpda^{2-}$-based homometallic EMACs reported in the past (Ni_5,[89] Cr_5,[90,91] Co_5 [92] and Ru_5 [93]), are pentametallic chains wrapped by four ligands and thus contain one more metal center and one more ligand as compared with **1Cl** and **1Br**. Quite remarkably, a similar situation is encountered in iron(II) complexes of tridentate dpa^-. Only two iron(II) centers are incorporated,[80,88] whereas with different metals the coordination capacity of the ligand is fully exploited to give Ni_3,[94,95] Cr_3,[84] Co_3,[83,85] Cu_3 [86,87] and Ru_3 [96] species. This behavior is difficult to understand on purely structural grounds, *e.g.* on the basis of ionic radii.

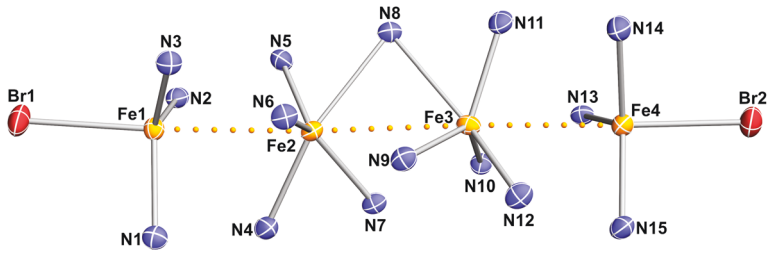

Fig. 4 Coordination geometry of the four Fe centers in **1Br** (right-handed enantiomer), drawn using the same color code as in Fig. 2. The dotted lines connecting the Fe centers do not indicate chemical bonds. Thermal ellipsoids are drawn at the 60% probability level.

Electrochemistry

Extensive, temperature dependent electrochemical measurements were carried out on **1Cl** and **1Br** in CH_2Cl_2 solution. The cyclic voltammogram of **1Cl** at −10 °C using 0.1 M TBACl as supporting electrolyte was presented previously in ref. 41 and shows four quasi-reversible signals spanning a potential range of 0.80 V (Fig. 5 and Table 2). **1Br** behaves similarly: its cyclic voltammogram at −13 °C (Fig. 5) consists of four consecutive redox signals (hereafter indicated as signals I, II, III, and IV at increasing potential values). The curves are stable and do not change with time using 0.1 M TBABr as supporting electrolyte. As found in **1Cl**, the peak-to-peak separation increases from signal I to IV and with the potential scan rate. The peak currents of all the signals are proportional to the square root of the scan rate (not shown). The electrochemistry of the complex consists of four quasi-reversible and diffusion controlled redox processes spanning a potential window of only 0.75 V, whereby the **1Br** complex shuttles between five oxidation states (Table 2). These four reversible ET processes will be hereafter indicated as ET-I, ET-II, ET-III and ET-IV and correspond to the ETs: $(Fe_4)^{8+} \rightleftarrows (Fe_4)^{9+}$, $(Fe_4)^{9+} \rightleftarrows (Fe_4)^{10+}$, $(Fe_4)^{10+} \rightleftarrows (Fe_4)^{11+}$, $(Fe_4)^{11+} \rightleftarrows (Fe_4)^{12+}$. The $E^{o\prime}$ values of corresponding ET steps (from ET-I to ET-IV) are much more negative in **1Cl**[41] than in **1Br**. The difference amounts to 0.110–0.235 V, depending on the redox step. Thus, from a thermodynamic point of view, chlorido ligands allow an easier oxidation of the Fe^{2+} ions than bromido ligands. This agrees with the higher Fe^{3+}-binding affinity of Cl^- with respect to Br^- and is consistent with experimental evidence gained during the syntheses (*i.e.*, **1Br** is less air-sensitive).

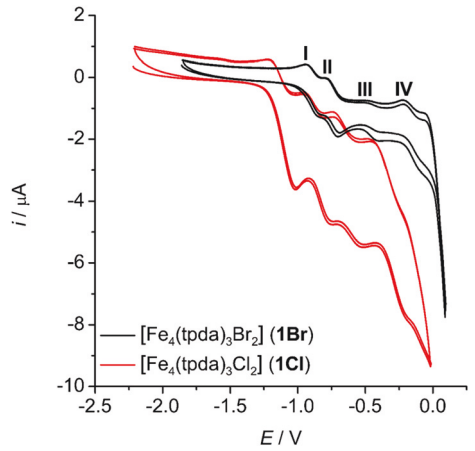

Fig. 5 Cyclic voltammogram of **1Br** (black line) and **1Cl** (red line). Conditions for **1Br**: GC working electrode, 0.1 M TBABr in CH_2Cl_2, scan rate 0.05 V s^{-1}, ferrocenium/ferrocene reference, T = −13 °C. Conditions for **1Cl**: GC working electrode, 0.1 M TBACl in CH_2Cl_2, scan rate 0.05 V s^{-1}, ferrocenium/ferrocene reference, T = −10 °C (data for **1Cl** are taken from ref. 41).

The $E^{o\prime}$ values of all redox steps in both complexes show a monotonic linear increase with increasing temperature from −13 to +3 °C (Fig. S7 and S8†). The calculated values of $\Delta S^{o\prime}_{rc}$ and $\Delta H^{o\prime}_{rc}$ are reported in Table S4.† $E^{o\prime}$ is made up of two opposite contributions: an enthalpic term which is negative

Table 2 Electrochemical data from CV for the consecutive ET processes of **1Br** (**1Cl**) in CH_2Cl_2 at −13 °C, using TBABr (TBACl) 0.1 M as base electrolyte[a]

	$E^{o\prime}$/V	$\Delta E^{o\prime}$/V	K_c	k_{ET}/cm s^{-1}
ET-I	−0.890 (−1.125)			0.00952 (0.00418)
		0.145 (0.270)	0.65×10^3 (1.73×10^5)	
ET-II	−0.745 (−0.855)			0.0102 (0.00341)
		0.302 (0.216)	7.21×10^5 (1.55×10^4)	
ET-III	−0.443 (−0.639)			0.00721 (0.00225)
		0.301 (0.316)	6.89×10^5 (1.35×10^6)	
ET-IV	−0.142 (−0.323)			0.00514 (0.00192)

[a] $E^{o\prime}$ = formal reduction potential (referenced to the ferrocenium/ferrocene redox couple), $\Delta E^{o\prime}$ = separation in $E^{o\prime}$ values of consecutive ET processes, K_c = comproportionation constant, k_{ET} = heterogeneous ET rate constant. The average errors on $E^{o\prime}$, $\Delta E^{o\prime}$, K_c and k_{ET} are ±0.002 V, ±0.004 V, ±12% and ±6%, respectively.

and predominant, and an entropic term which is positive and smaller in magnitude. The enthalpic contribution decreases progressively in magnitude from ET-I to ET-IV, although the $\Delta H_{rc}^{\circ\prime}$ values are markedly different in **1Cl** and **1Br**. The entropic contribution $\Delta S_{rc}^{\circ\prime}$ in ET-I is much higher than in the remaining ET steps, which conversely entail very similar entropic contributions. This is probably related to the fact that the reorganization effect of the solvent around the complex is much more extensive in ET-I than in the other ET steps. In fact, the first oxidation (ET-I) transforms a neutral species into a monopositive one, while ET-II to ET-IV increase the charge of an already charged species. Other related iron complexes exhibit similar electrochemical behavior.[46,97]

In **1Br** the observed differences in $E^{\circ\prime}$ values for consecutive ET processes ($\Delta E^{\circ\prime}$) correspond to moderate (ET-I/ET-II) or large (ET-II/ET-III and ET-III/ET-IV) comproportionation constants $K_c = \exp\left[nF\left(E_1^{\circ\prime} - E_2^{\circ\prime}\right)/RT\right]$, whose values are shown in Table 2.[98,99] The order of magnitude of K_c in **1Br** spans the range 10^3–10^6 as compared with 10^4–10^6 in **1Cl**. The data indicate high thermodynamic stability toward disproportionation for the mixed-valence species $(Fe_4)^{10+}$ and $(Fe_4)^{11+}$ derived from **1Br**, which might become synthetically accessible,[100] whereas $(Fe_4)^{9+}$ is much less stable. Interestingly, replacing Cl^- axial ligands with Br^- affects to the largest extent the stability of the monooxidized $(Fe_4)^{9+}$ species, whose K_c value undergoes a more than 200-fold decrease from **1Cl** to **1Br**.

The enthalpic $\left(\Delta H_c^{\circ\prime}\right)$ and entropic $\left(\Delta S_c^{\circ\prime}\right)$ contributions to K_c were determined by recording the temperature dependence of K_c and applying the van't Hoff equation (Fig. S9†). The results, presented in Table S5,† reveal that in both **1Br** and **1Cl** the major contribution to K_c is of enthalpic origin, although a significant, albeit minor, entropic contribution is observed for the species $(Fe_4)^{9+}$. The other mixed-valence species show negligible entropic contributions to K_c. The observed difference is due to the very positive value of $\Delta S_{rc}^{\circ\prime}$ of ET-I (see above).

The heterogeneous k_{ET} values for signals I and II of **1Br** are rather similar, but then progressively decrease from signal II to IV (*i.e.* with increasing oxidation state and charge of the complex, see Table 2) probably due to a progressive increase in the reorganization energy λ, as already observed for other mixed-valence complexes.[101] A similar behavior is shown by the chloro derivative **1Cl**, although the differences in k_{ET} values are much less noticeable. The k_{ET} values of corresponding ET steps are always higher in **1Br** than in **1Cl**, suggesting different reorganization energies.

Mössbauer spectroscopy

Mössbauer spectra collected on **1Cl** and **1Br** at 10 and 77 K (Fig. 6 and 7) suggest similar electronic structures in the two complexes. Since all four Fe centers are crystallographically independent in the solid state, it is expected that each of them would exhibit a quadrupole doublet. However, the Mössbauer spectra of **1Cl** and **1Br** allowed the resolution of only two distinct quadrupole doublets (sub-spectra 1 and 2), with equal intensities and spectral parameters consistent with HS Fe^{2+} (Table 3).[102] Hence, the four Fe sites can be partitioned into

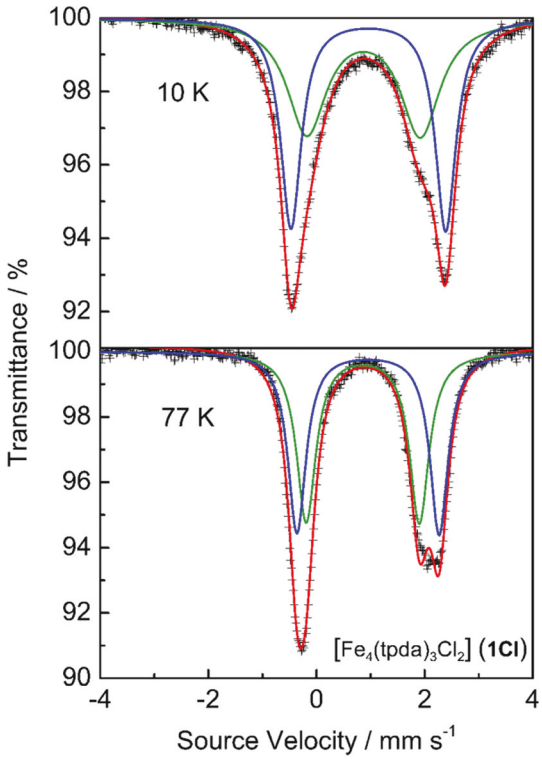

Fig. 6 Mössbauer data for **1Cl** at 10 K (top) and 77 K (bottom). The green line corresponds to sub-spectrum 1, the blue line to sub-spectrum 2, the red line to the overall fit, and the black crosses to the experimental data. Best-fit parameters for both temperatures are listed in Table 3.

two chemically distinct pairs, with unresolvable differences in Mössbauer parameters within each pair. The much increased linewidth of sub-spectrum 1 at 10 *vs.* 77 K may actually hint at enhanced chemical inequivalence within the pair at 10 K. In fact, lowering temperature has been shown to lead to lower-symmetry structures in related Fe-containing chain compounds.[33] Such a structural change, or more likely small differences in the second order Doppler effect for these Fe sites may be responsible or contribute to the observed broadness of the sub-spectrum 1 at 10 K. The best-fit parameters to the 10 and 77 K datasets are otherwise similar, suggesting that the Fe centers undergo no gross changes in geometry, oxidation or spin state in the explored temperature range. We propose that sub-spectrum 1 arises from the internal Fe sites (Fe2 and Fe3), whereas the doublet with the higher ΔE_Q (sub-spectrum 2) is due to the terminal Fe sites (Fe1 and Fe4). Our assignment is supported by the Mössbauer behavior of the bimetallic Co^{2+}–Fe^{2+} complex [CoFe(py$_3$tren)Cl] (**8**), which features an FeN_3Cl chromophore and no metal–metal bond (H_3py_3tren = *N*,*N*,*N*-tris(2-(2-pyridylamino)ethyl)amine). At 80 K, the HS Fe^{2+} ion in **8** has δ = 0.88 mm s^{-1}, ΔE_Q = 2.62 mm s^{-1} and FWHM = 0.35 mm s^{-1}.[103] The quadrupole splitting is thus practically identical to that of sub-spectrum 2 in **1Cl** at 77 K (Table 3), although the isomer shift is roughly intermediate between sub-spectra 1 and 2. The diiron(II) complex [Fe_2(py$_3$tren)Cl],

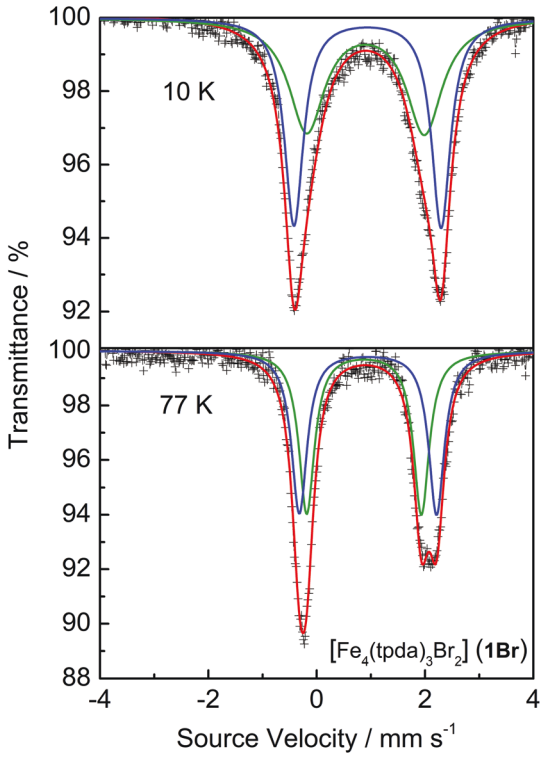

Fig. 7 Mössbauer data for **1Br** at 10 K (top) and 77 K (bottom). Same color code as in Fig. 6. Best-fit parameters for both temperatures are listed in Table 3.

also reported in ref. 103, unfortunately cannot be used to support our assignment, because the Fe–Fe bond strongly modifies its Mössbauer behavior. Importantly, no Fe^{3+} impurities are detectable by Mössbauer spectroscopy in either **1Cl** or **1Br**. Therefore, our synthetic procedure (see above), in addition to being reproducible and well tested, is successful in preventing any oxidation of the Fe^{2+} ions.

DC magnetic properties and AOM calculations

The DC magnetic response of a polycrystalline sample of **1Br**·2.3CH_2Cl_2·Et_2O is presented in Fig. 8(a). The value of $\chi_M T$ (χ_M = molar magnetic susceptibility) at 300 K is 16.4 emu K mol^{-1}. Because of the absence of metal–metal bonds, it is meaningful to compare this value with the cumulative Curie constant for four localized and noninteracting $S = 2$ spins, which is significantly lower (12.0 emu K mol^{-1} with $g = 2.00$). On lowering temperature, the $\chi_M T$ product undergoes a small increase up to its maximum value at 100 K (17.3 emu K mol^{-1}). With further cooling, it drops rapidly to 2.4 emu K mol^{-1} at 2 K, signaling a weakly magnetic ground state. This is also reflected by isothermal M_M *vs.* H curves recorded at 2, 4, and 8 K (M_M is molar magnetization). At the highest available field (H = 70 kOe), the average value of M_M reaches 9.3 $N_A\mu_B$, which is about 60% of the saturation value of 16.0 $N_A\mu_B$ expected for four noninteracting $S = 2$ spins with $g = 2.00$ (N_A is Avogadro's constant and μ_B is the Bohr magneton). This behavior closely mirrors that found in **1Cl**·2.6CH_2Cl_2·0.84Et_2O (Fig. 8(b)), which was recently analyzed by us using a local-site model and treating LF effects in a simplified fashion within the AOM.[41] At this level of theory, the approximately C_{3v} coordination geometry of Fe1 and Fe4 yields an unquenched first-order orbital momentum and a large easy-axis anisotropy roughly parallel to Z. By contrast, Fe2 and Fe3 have a well-isolated $S = 2$ orbital singlet and an easy-axis anisotropy directed roughly normal to Z. This analysis showed that the measured $\chi_M T$ *vs.* T curve is substantially different from the predicted response of four uncoupled Fe^{2+} centers and can only be modelled by introducing super-exchange interactions. Using $J\hat{\mathbf{S}}_i\cdot\hat{\mathbf{S}}_j$ convention for the Heisenberg Hamiltonian, the best model entails (a) ferromagnetic interactions ($J < 0$) within the Fe1–Fe2 and Fe3–Fe4 pairs, which dominate around room temperature, and (b) weaker antiferromagnetic coupling ($J_{eff} > 0$) between the two pairs (treated in the mean-field approximation) to reproduce the $\chi_M T$ drop at low T.[41] For comparison, exactly the same strategy was applied to **1Br**·2.3CH_2Cl_2·Et_2O, as detailed in ESI Note 4.† The best-fit parameters so obtained are as follows: $J = -14.1(3)$ cm^{-1}, $J_{eff}/g_{av}{}^2 = 0.315(4)$ cm^{-1} and TIP = 3.39(16) × 10^{-3} emu mol^{-1} (g_{av} is the temperature-independent average g-factor of the Fe_2 unit). The best-fit curve is drawn in Fig. S12.† As compared with **1Cl**·2.6CH_2Cl_2·0.84Et_2O ($J = -21.4(4)$ cm^{-1}, $J_{eff}/g_{av}{}^2 = 0.345(7)$ cm^{-1} and TIP = 2.1(2) × 10^{-3} emu mol^{-1}), the interdimer interaction is similar, while the intradimer ferromagnetic coupling is ~35% weaker.

Ab initio calculations

The single-ion properties in complexes **1Cl** and **1Br** were investigated by CASSCF-NEVPT2-SO calculations (see Experimental section). The treatment showed that, at variance with AOM results, quenching of first-order orbital momentum is substantial even for the terminal centers Fe1 and Fe4. Deviations from threefold symmetry in their coordination environment are in fact sufficient to split the ^5E term by a few hundreds of wavenumbers. Upon application of SO coupling, the five lowest-

Table 3 Best-fit Mössbauer parameters for **1Cl** and **1Br** at 77 K (10 K).[a] Standard deviations are estimated to be ~0.01 mm s^{-1}

	Sub-spectrum	δ (mm s^{-1})	ΔE_Q (mm s^{-1})	FWHM (mm s^{-1})
$[Fe_4(tpda)_3Cl_2]$ (**1Cl**)	1	0.86 (0.87)	2.09 (2.10)	0.43 (0.88)
	2	0.95 (0.96)	2.63 (2.86)	0.41 (0.46)
$[Fe_4(tpda)_3Br_2]$ (**1Br**)	1	0.87 (0.90)	2.12 (2.17)	0.35 (0.80)
	2	0.95 (0.94)	2.54 (2.72)	0.35 (0.42)

[a] Reduced χ^2: 1.677 (0.793) for **1Cl** and 0.577 (0.747) for **1Br**.

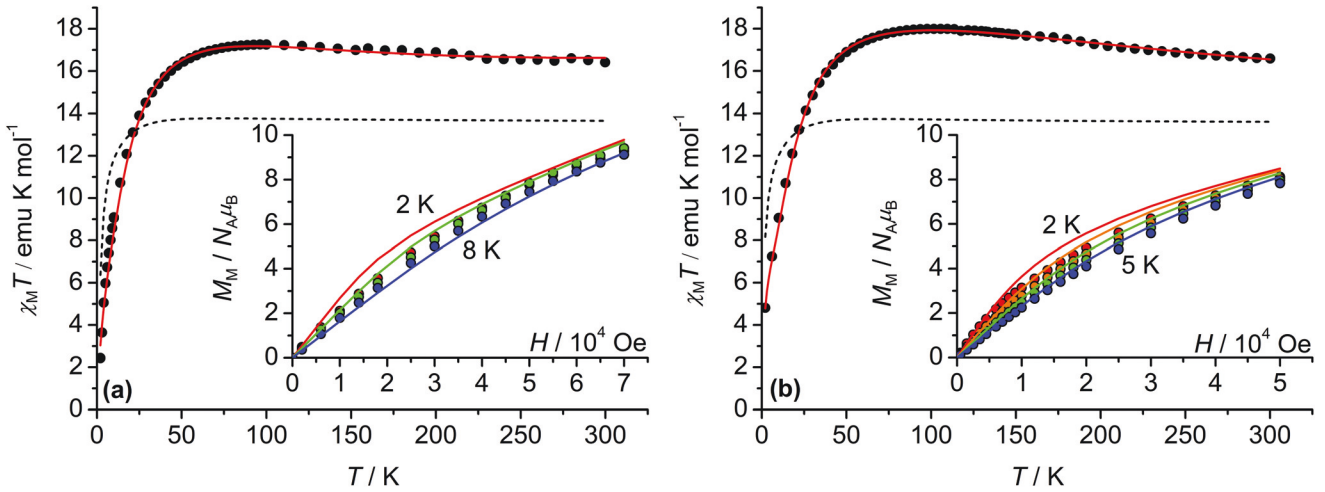

Fig. 8 DC magnetic response of polycrystalline samples of **1Br**·2.3CH_2Cl_2·Et_2O (a) and **1Cl**·2.6CH_2Cl_2·0.84Et_2O (b). The black dots in the main panels are the experimental temperature-dependent $\chi_M T$ data measured at H = 10 kOe (a) or 1 kOe (b). The insets show isothermal M_M *vs.* H data recorded (a) at 2, 4, and 8 K (red, green and blue dots, respectively), and (b) at 2, 3, 4, and 5 K (red, orange, green and blue dots, respectively). The solid curves provide the best-fit with *ab initio* approach using model m**1Br**D in (a) and model m**1Cl**D in (b). The dashed lines are the simulated magnetic responses of four uncoupled HS iron(II) ions, with single-ion parameters fixed at the values obtained by *ab initio* calculations. Experimental data in (b) are taken from ref. 41.

lying states are separated from excited states by at least 300–350 cm^{-1} except for Fe4 in **1Cl** (240 cm^{-1}) (Tables S9 and S10†). The situation is similar to that encountered in mononuclear iron(II) pyrrolide complexes, featuring a quasi-threefold symmetric FeN_3N coordination environment.[104–106] The five lowest-lying levels of the *i*-th metal ion were then mapped onto the single-ion spin Hamiltonian:

$$\hat{H}_i = \hat{\mathbf{S}}_i \cdot \bar{\bar{D}}_i \cdot \hat{\mathbf{S}}_i + \mu_B \mathbf{B} \cdot \bar{\bar{g}}_i \cdot \hat{\mathbf{S}}_i \quad (3)$$

where $\mathbf{S}_i$ is the spin vector (S_i = 2), $\bar{\bar{D}}_i$ and $\bar{\bar{g}}_i$ are the single-ion ZFS and g tensors, respectively, and $\mathbf{B}$ is the applied magnetic field. This showed that the anisotropy of Fe1 and Fe4 is of the easy-axis type (D_i < 0) with $|D_i|$ = 11–19 cm^{-1} (Table 4). A significant rhombic anisotropy is predicted, with $|E_i/D_i|$ = 0.05–0.18 and the intermediate direction lying close to the Fe1–N1 and Fe4–N13 bonds. The two inner metals, Fe2 and Fe3, display a very distorted coordination environment and attain an orbitally nondegenerate S_i = 2 electronic state as well. However, their anisotropy is of the hard-axis type (D_i > 0) with D_i = 8–10 cm^{-1} and $|E_i/D_i|$ = 0.06–0.21 in eqn (3) (Table 4). Interestingly, all four metal ions have their main anisotropy axes directed close to the chain axis, as pictorially shown in Fig. 9. Therefore, the terminal and internal Fe^{2+} ions have approximately collinear main anisotropy axes, but opposite anisotropies, with a preference of the spins at terminal (internal) sites to align parallel (perpendicular) to Z. Notice that the AOM also predicted a qualitatively similar tendency, but with a different origin: an orbitally degenerate ground term for Fe1 and Fe4, and an easy-axis anisotropy normal to Z for Fe2 and Fe3.

Overall, Tables 4 and S11† and Fig. 9 indicate that the single-ion $\bar{\bar{D}}_i$ and $\bar{\bar{g}}_i$ tensors are very similar in the two derivatives, in terms of both magnitude and orientation. Knowledge of these single-ion properties allowed modelling the magnetic behavior of **1Cl** and **1Br** without risk of overparameterization. First, PHI v3.1.5 software[77] was used to calculate the $\chi_M T$ *vs.* T response for the four noninteracting HS Fe^{2+} ions with single-ion parameters fixed at the values obtained by *ab initio* calculations. The result (dashed lines in Fig. 8) is very far from experimental data and further confirms the existence of magnetic interactions among metal ions.

Table 4 Single-ion ZFS parameters and g-factors of **1Cl** and **1Br** from *ab initio* calculations

	$[Fe_4(tpda)_3Cl_2]$ (**1Cl**)		$[Fe_4(tpda)_3Br_2]$ (**1Br**)	
	D_i, E_i [a] (cm^{-1})	$g_{1,i}$, $g_{2,i}$, $g_{3,i}$ [b]	D_i, E_i [a] (cm^{-1})	$g_{1,i}$, $g_{2,i}$, $g_{3,i}$ [b]
Fe1	−11.32, −1.94	1.998, 2.125, 2.311	−12.02, −2.18	1.994, 2.134, 2.324
Fe2	9.61, 1.95	2.000, 2.101, 2.201	9.62, 2.05	2.001, 2.099, 2.203
Fe3	7.81, 0.50	2.007, 2.111, 2.131	7.68, 0.51	2.007, 2.108, 2.132
Fe4	−18.97, −0.92	1.934, 2.067, 2.425	−17.43, −1.49	1.962, 2.100, 2.406

[a] Axial and rhombic ZFS parameters of Fe*i*. [b] Principal values of the $\bar{\bar{g}}_i$ tensor of Fe*i*, listed in order of increasing magnitude.

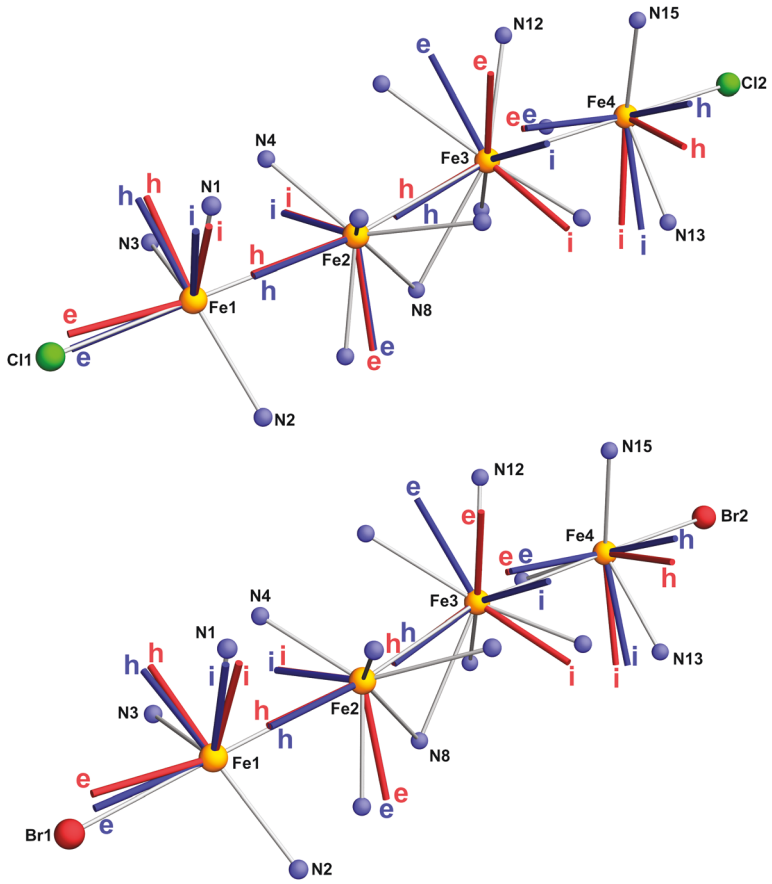

Fig. 9 Principal directions of single-ion $\bar{\bar{D}}_i$ (blue) and $\bar{\bar{g}}_i$ (red) tensors obtained by *ab initio* calculations on **1Cl** (upper panel) and **1Br** (lower panel). e = easy, i = intermediate, h = hard direction.

We then wrote a new spin Hamiltonian $\hat{H}$ as the sum of single-ion spin Hamiltonians $\hat{H}_i$ (eqn (3)) and of a Heisenberg Hamiltonian, which accounts for super-exchange interaction between the *i*- and *j*-th localized spin centers through isotropic coupling constant J_{ij} (Scheme 3). Both nearest-neighbor (J_{12}, J_{23}, J_{34}) and next-nearest-neighbor (J_{13}, J_{24}) couplings were included, setting $J_{13} = J_{24} = J'$ for simplicity.

$$\hat{H} = \sum_{i=1}^{4} \hat{H}_i + J_{12}\hat{\mathbf{S}}_1 \cdot \hat{\mathbf{S}}_2 + J_{34}\hat{\mathbf{S}}_3 \cdot \hat{\mathbf{S}}_4 + J_{23}\hat{\mathbf{S}}_2 \cdot \hat{\mathbf{S}}_3 + J'(\hat{\mathbf{S}}_1 \cdot \hat{\mathbf{S}}_3 + \hat{\mathbf{S}}_2 \cdot \hat{\mathbf{S}}_4) \quad (4)$$

Several models, labelled as m**1X**A, m**1X**B, *etc.* (X = Cl, Br), were tested for their ability to simultaneously account for $\chi_M T$ *vs.* T and M_M *vs.* H data. The models differ in the constraints applied to J_{ij} values as well as in the refinement of a TIP correction. A detailed account of the procedure is available in ESI Note 5, in Tables S12–S14 and in Fig. S13–S17.†

We contend that m**1Cl**D (J_{12} = −51.4(10), J_{34} = −9.43(5), and J_{23} = 4.319(7) cm^{-1}) and m**1Br**D (J_{12} = −26.8(14), J_{34} = −4.61(15), J_{23} = 4.19(3) cm^{-1}) are the most plausible models for the two derivatives, with a J_{12} constant 5–6 times more ferromagnetic than J_{34} (Fig. 8). Notice that the average magnitude of the two coupling constants is smaller in **1Br** (−15.7 cm^{-1}) than in **1Cl** (−30.4 cm^{-1}), as found in our simplified treatment based on AOM. Furthermore, the two models entail remarkably similar values of J_{23} (4.2–4.3 cm^{-1}), again in accordance with the almost superimposable structures of the two derivatives and with AOM-based treatment.

We now analyze in detail the lowest-lying spin levels in the two complexes, as resulting from the parameters ($\bar{\bar{D}}_i$ and $\bar{\bar{g}}_i$ tensors, and best-fit J_{ij} values) of models m**1Cl**D and m**1Br**D. At H = 0, the lowest-energy states are closely-spaced non-Kramers doublets (hereafter referred to as *pseudo*-doublets), which however do not follow the pattern typical of a well-isolated total spin state undergoing predominantly axial ZFS (Fig. S18 and S19†). Each of these pseudo-doublets can be approximated to an $\tilde{S}$ = 1/2 *pseudo*-spin with an anisotropic

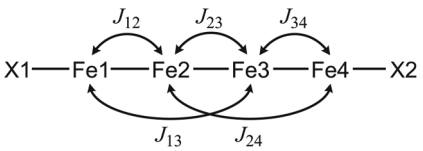

Scheme 3 Definition of super-exchange coupling constants J_{ij} in complexes **1Cl** and **1Br**. Terminal ligands X1 and X2 can be either Cl (**1Cl**) or Br (**1Br**).

g-tensor (principal components g_1, g_2 and g_3 in order of increasing magnitude).[77] Notice that in non-Kramers systems pseudo-doublets have vanishing values of g_1 and g_2. The ground doublet in **1Cl** (**1Br**) has $g_3 \sim 7.6$ (6.4) in a direction (z_3) at about 29° (44°) from Z. This g_3 value corresponds to magnetic moment projections of $\pm 3.8\mu_B$ ($\pm 3.2\mu_B$) and the ground doublet is thus only weakly magnetic. The first-excited doublet lies about 2.5 (4.6) cm^{-1} higher in energy. It has $g_3' \sim 9.1$ (11.3) in a direction (z_3') that forms an angle of about 26° (17°) with Z and is consequently more magnetic than the ground doublet. Fig. S18 and S19† present the expected Zeeman splittings when a magnetic field up to 10 kOe is applied along z_3.

The local spin components in the four lowest-lying states (1 to 4, in order of increasing energy) have been computed for H = 1 kOe directed along z_3 or z_3'. The results for the ground doublet of **1Cl** are presented in vectorial form and superimposed to the X-ray molecular structure in Fig. 10. Similar views for the first-excited doublet of **1Cl** and for states 1 to 4 of **1Br** are available as Fig. S20–S22.†

The states comprised in each doublet have roughly opposite components of the local spins, as expected; furthermore, spin components are substantial and reveal a noncollinear spin arrangement (Table S15†). Looking at state 1 (Fig. 10), the large ferromagnetic coupling between Fe1 and Fe2 and the antiferromagnetic coupling of Fe2 to Fe3 limit noncollinearities between neighboring spins to less than 20°. Moreover, spins at these sites form large angles with the chain axis (Table S15†). This arrangement is understood as a consequence of the fact that the magnetic anisotropies of Fe1 and Fe2 are comparable in magnitude, roughly collinear but opposite in sign. The coupled state of the pair is thus only weakly anisotropic and the spins are torqued away from Z under the influence of hard-axis Fe3 and of the antiferromagnetic J_{23} interaction. Due to the large $|D|$ value of the terminal metal Fe4 and the weak ferromagnetic interaction between Fe3 and Fe4, the spin on Fe4 lies close to its local easy direction and forms a substantial angle with the spin on Fe3 (Fig. 10 and Table S15†). Notice that noncollinearities within the Fe1,Fe2 and Fe3,Fe4 pairs are enhanced in **1Br**, which features smaller $|J_{12}|$ and $|J_{34}|$ values (Fig. S21 and Table S15†). As a final observation, the spins on Fe1, Fe2, and Fe3 are roughly orthogonal to z_3 and contribute only marginally to the magnetic moment in state 1, which is primarily determined by Fe4.

The origin of the weakly magnetic pseudo-doublet ground state is clearly the competition between the large, noncollinear single-ion anisotropies and super-exchange interactions. For dominant super-exchange couplings, the alternating signs of J_{ij} constants across the molecule (Scheme 3) would afford a nonmagnetic ground state with S = 0 total spin, irrespective of local anisotropies. In the complexes under study, this strong-exchange regime[16] is not reached and the ground state is magnetic – albeit weakly. To ascertain the role of noncollinear anisotropies, test calculations were performed using the best-fit J_{ij} values of model m**1Cl**D but averaging all $\bar{\bar{D}}_i$ and $\bar{\bar{g}}_i$ tensors to axial symmetry and aligning their main axes with Z. With this operation, the g_3 value for the ground pseudo-doublet drastically decreases from 7.6 to 0.62. The new zero-field wavefunctions are predominantly (>50%) constituted by the pairs of product states $|-2,-1,+1,+2\rangle$, $|+2,+1,-1,-2\rangle$ and $|-2,-2,+2,+2\rangle$, $|+2,+2,-2,-2\rangle$, with equal weights within each pair (product states are labelled with the M_S quantum numbers of the four ions). The unequal g-factors along Z are the reason for the residual magnetic response of the ground pseudo-doublet, which would otherwise be perfectly nonmagnetic (g_3 = 0). The occurrence of a magnetic ground state is consistent with the observation of SMM properties in both derivatives, as presented in the next section.

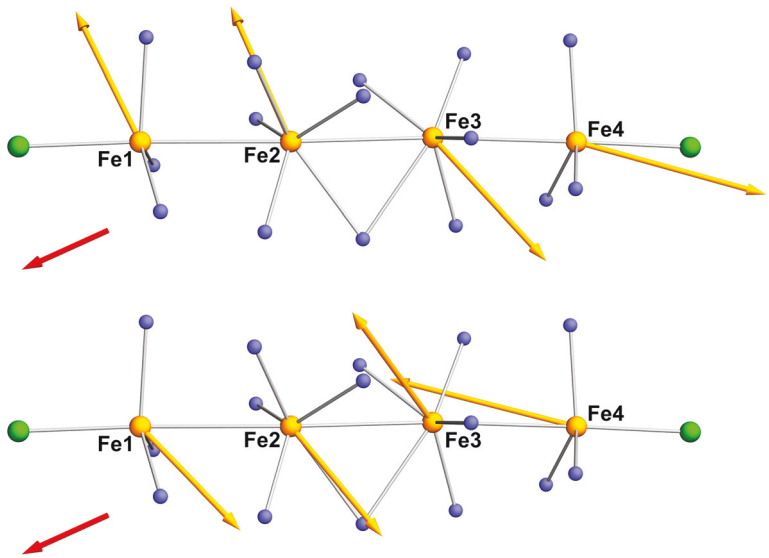

Fig. 10 Local spin components (orange arrows, drawn on an arbitrary scale) in the ground doublet of **1Cl** when a 1 kOe magnetic field (red arrow) is applied along the direction of maximum Zeeman splitting (z_3). The upper and lower panels picture states 1 and 2, respectively. Color code: orange, Fe; blue, N; green, Cl.

AC magnetic studies

A crystalline sample of **1Cl**·2.6CH_2Cl_2·0.84Et_2O, investigated up to ν = 1500 Hz, showed the onset of slow relaxation of the magnetization below 2.8 K when a small static field (H_{DC} = 2 kOe) was applied, but no detectable out-of-phase signal at H_{DC} = 0.[41] AC susceptibility measurements were also performed on a polycrystalline sample of **1Br**·2.3CH_2Cl_2·Et_2O up to ν = 9980 Hz. Preliminary scans at 2.0 K for H_{DC} values between 0 and 2.5 kOe revealed that the compound features slow relaxation of the magnetization even in zero DC field (Fig. S23†). The frequency dependence of the in-phase (χ_M') and out-of-phase (χ_M'') components of molar magnetic susceptibility does not change significantly above 2 kOe. Complete sets of frequency-

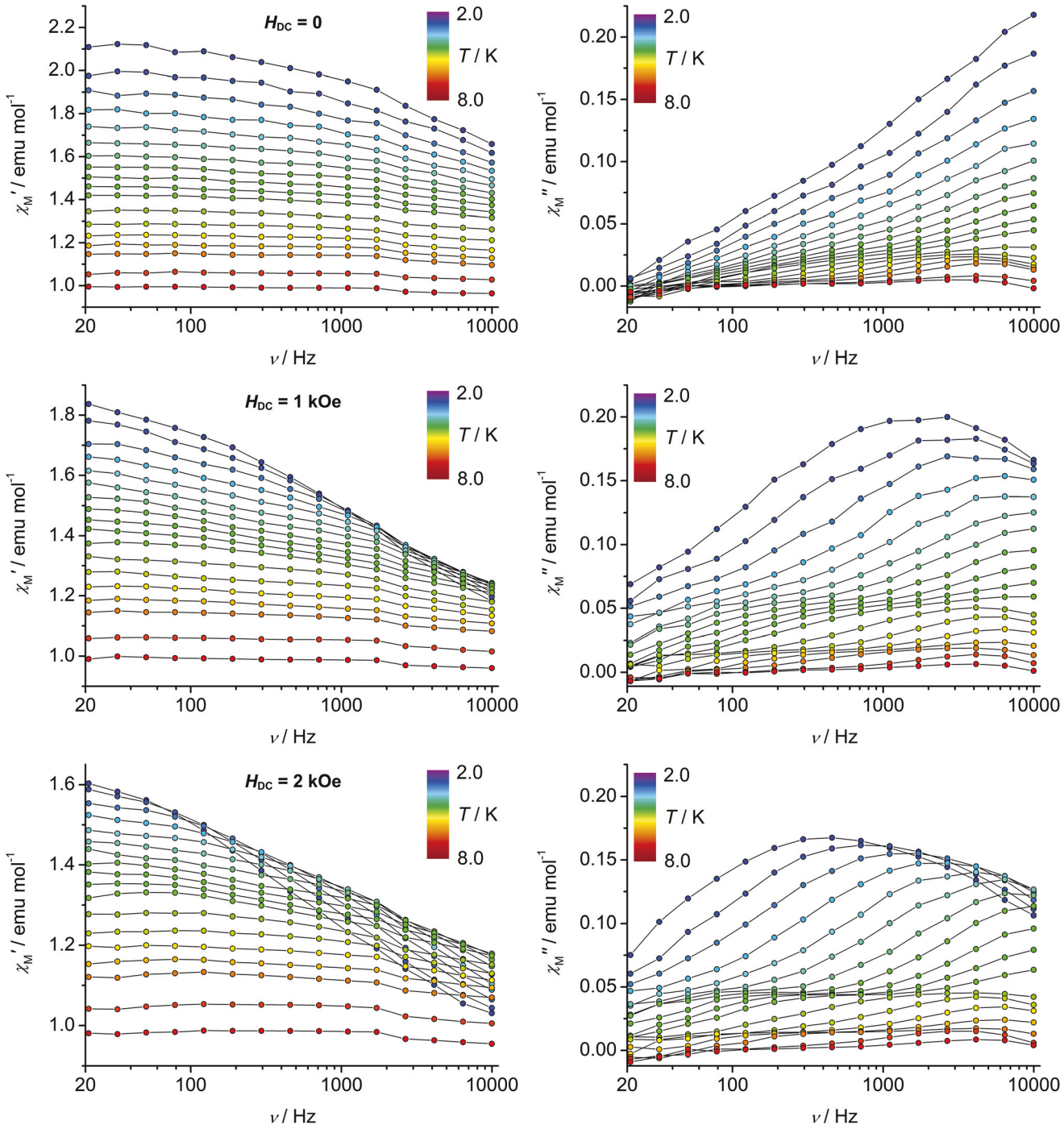

Fig. 11 Frequency dependence of the in-phase (χ_M', left panels) and out-of-phase (χ_M'', right panels) components of molar magnetic susceptibility for **1Br**·2.3CH_2Cl_2·Et_2O at T = 2.0, 2.2, 2.4, 2.6, 2.8, 3.0, 3.2, 3.4, 3.6, 3.8, 4.0, 4.4, 4.8, 5.2, 5.6, 6.0, 7.0, and 8.0 K. Measurements were carried out with a DC field of 0 (top), 1 (middle), and 2 kOe (bottom).

dependent data were then recorded at 0, 1, and 2 kOe for temperatures between 2.0 and 8.0 K. In zero DC field, the onset of slow relaxation of the magnetization was clearly detected below 4.0 K, where each isothermal $\chi_M''(\nu)$ curve is a monotonic increasing function (Fig. 11), with no detectable maximum in our accessible frequency range. Therefore the χ_M'' *vs.* ν curves could not be fitted with the generalized Debye model.[16] An alternative method,[107,108] employed also to fit the AC data of **1Cl**·2.6CH_2Cl_2·0.84Et_2O,[41] was used which allows a rough estimate of U_{eff}/k_B and τ_0 by applying eqn (5):

$$\ln(\chi_M''/\chi_M') = \ln(\omega\tau_0) + E_a/(k_BT) \quad (5)$$

where $\omega = 2\pi\nu$, $E_a \approx U_{eff}$ and k_B is the Boltzmann constant. Eqn (5) is valid assuming that only one characteristic Debye relaxation process is present, with one time constant and one energy barrier. A linear regression on $\ln(\chi_M''/\chi_M')$ *vs.* $1/T$ data between 2.0 and 4.0 K was then performed for each ν value ranging from 78.7 to 9980 Hz (Fig. S24†). The values U_{eff}/k_B = 5.4(4) K and $\tau_0 = 1.1(8) \times 10^{-6}$ s were obtained by averaging the best-fit slopes (E_a/k_B) and intercepts ($\ln(\omega\tau_0)$), respectively, at different frequencies (the numbers in parentheses are the associated standard deviations).

Upon application of a DC field the magnetic relaxation slows down and clear maxima appear in isothermal χ_M'' *vs.* ν curves recorded at $T \leq 3.0$ K (Fig. 11). The nonzero H_{DC} is likely to reduce the efficiency of under-barrier relaxation processes, such as quantum tunneling of the magnetization (QTM), which are expected because of the significant rhombicity of the structure.[16,109] The standard treatment is then applicable, based on extended Debye model[16,110,111] and on eqn (6)–(8),

$$\chi_M(\omega) = \chi_{M,S} + \frac{(\chi_{M,T} - \chi_{M,S})}{1 + (i\omega\tau)^{1-\alpha}} \quad (6)$$

$$\chi_M''(\omega) = (\chi_{M,T} - \chi_{M,S})\frac{(\omega\tau)^{1-\alpha}\cos(\pi\alpha/2)}{1 + 2(\omega\tau)^{1-\alpha}\sin(\pi\alpha/2) + (\omega\tau)^{2-2\alpha}} \quad (7)$$

$$\chi_M'(\omega) = \chi_{M,S} + (\chi_{M,T} - \chi_{M,S})\frac{1 + (\omega\tau)^{1-\alpha}\sin(\pi\alpha/2)}{1 + 2(\omega\tau)^{1-\alpha}\sin(\pi\alpha/2) + (\omega\tau)^{2-2\alpha}} \quad (8)$$

where $\chi_{M,T}$ and $\chi_{M,S}$ are the isothermal and adiabatic susceptibilities, respectively, τ is the average relaxation time and α determines the width of the distribution of relaxation times (α = 0 corresponds to a single relaxation process, while α = 1 to an infinitely wide distribution). Isothermal χ_M'' and χ_M' *vs.* ν curves were simultaneously fitted with eqn (7) and (8), in order to cross-check the two experimental datasets and obtain more reliable results. The best-fit parameters (τ, α, $\chi_{M,T}$ and $\chi_{M,S}$) for the two different static fields are reported in Tables S16 and S17.† In both cases, the relaxation times decrease with increasing temperature, presumably due to the progressive enhancement of thermally activated relaxation processes. The use of a 2 kOe static field leads to approximately three times slower relaxation than at H_{DC} = 1 kOe. The α parameter does not follow a straightforward trend, but for H_{DC} = 1 kOe (2 kOe) it ranges between 0.51–0.63 (0.44–0.51). Its substantial value (≈0.5) highlights a very broad distribution of relaxation times. From Fig. 12 it is evident that the $\ln(\tau)$ *vs.* $1/T$ plots at 1 and 2 kOe do not follow a linear trend. Therefore, slow relaxation of the magnetization cannot be described solely by a multistep thermally activated relaxation processes (Orbach mechanism), where τ exponentially increases with decreasing T and follows the expression $\tau = \tau_0 \exp[U_{eff}/(k_BT)]$. The temperature dependences of $\ln(\tau)$ at 1 and 2 kOe were simultaneously fitted to eqn (9), which accounts for Orbach and QTM relaxation mechanisms but disregards Raman relaxation:

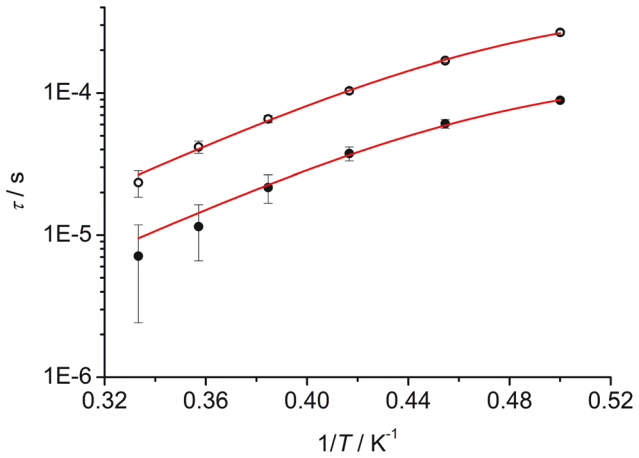

Fig. 12 Temperature dependence of the relaxation time of **1Br**·2.3CH_2Cl_2·Et_2O (τ, in $\log_{10}$ scale) at H_{DC} = 1 kOe (solid dots) and 2 kOe (open dots), along with the best-fit curves (red lines).

$$\tau = \{\tau_0^{-1}\exp[-U_{eff}/(k_BT)] + \tau_{QTM}^{-1}\}^{-1} \quad (9)$$

In eqn (9), τ_{QTM} is the relaxation time associated to QTM mechanism and only U_{eff} is assumed to be independent of H_{DC}. The calculated best-fit parameters are: at H_{DC} = 1 kOe, $\tau_0 = 1.9(6) \times 10^{-8}$ s, $\tau_{QTM} = 1.44(11) \times 10^{-4}$ s; at H_{DC} = 2 kOe, $\tau_0 = 5.2(16) \times 10^{-8}$ s, $\tau_{QTM} = 4.4(4) \times 10^{-4}$ s; U_{eff}/k_B = 18.9(8) K. This value of U_{eff} is ~3.5 times larger than that estimated in zero DC field, and is also larger than found in **1Cl** at 2 kOe (10.1 (1.3) K).[41]

Conclusions

In this work we have described and compared the solution and solid-state properties of two tetrairon-based EMACs supported by oligo-*α*-pyridylamido ligands and capped by halide ligands: **1Cl** and **1Br**. The complexes contain exclusively iron (II) centers, as most directly supported by Mössbauer spectroscopy, and undergo four consecutive quasi-reversible one-electron oxidations in dichloromethane solution. The DC magnetic properties indicate a weakly magnetic ground state in both derivatives. Slow relaxation of the magnetization is never-

theless detected in AC measurements, with **1Br** displaying SMM behavior even in zero static field. To aid the analysis of magnetic data, a local-site model was assumed and the single-ion properties were evaluated by *ab initio* (CASSCF-NEVPT2-SO) methods. The results showed that in these stringlike complexes the terminal metal centers (Fe1 and Fe4) have a negative D parameter whereas the internal ones (Fe2 and Fe3) have a positive D, corresponding to predominantly easy- and hard-axis magnetic anisotropies, respectively. Due to the significant deviations from D_3 molecular symmetry, however, different anisotropies are predicted for the two terminal metals and, to a lesser extent, for the internal ones; in addition, single-ion magnetic anisotropies display significant rhombic distortions with $|E/D|$ up to 0.2 and noncollinear principal axes. These local anisotropies compete with super-exchange interactions, which turn out to be ferromagnetic within the Fe1,Fe2 and Fe3,Fe4 pairs and antiferromagnetic between Fe2 and Fe3. Since the strong-exchange regime[16] typical of most polynuclear molecular magnets is not attained, the ground state is a non-Kramers doublet featuring a highly noncollinear spin arrangement.

In conclusion, the large Fe···Fe separations and the super-exchange patterns found in **1Cl** and **1Br** yield weak-to-moderate ferromagnetic couplings accompanied by antiferromagnetic contributions that severely plague SMM behavior. Additionally, the different coordination pockets available in these EMACs lead to opposite and partially cancelling local anisotropies. Therefore, the formation of metal–metal bonds seems requisite to stabilize well-isolated ground spin states in iron(II)-based EMACs.[42] Instilling a negative D parameter in the ground state is a second mandatory task for the design of metal–metal bonded SMMs. A recent study[112] on a dimeric system has clearly shown that local-site models are of limited utility to accomplish this task. In fact, the reorganization of MO energies upon metal–metal bond formation can trigger a strikingly different anisotropy as compared with that predicted by a localized model. An alternative strategy to strengthen ferromagnetic interactions in iron-based EMACs without Fe–Fe bonds is the design of mixed-valence species, in which double-exchange coupling is operative.[16,113,114] The rich electrochemistry of the herein reported iron(II) derivatives suggests that partially-oxidized derivatives may be chemically accessible and work is currently underway in this direction.

Conflicts of interest

There are no conflicts of interest to declare.

Acknowledgements

JFB thanks the US National Science Foundation for funding under CHE-1953924. The purchase of the Bruker ULTRAFLEX™ III in 2008 was partially funded by NIH NCRR 1S10RR024601-01 Award to the Department of Chemistry of UW-Madison. All co-authors thank Nathalie Guihery (Université Paul Sabatier, Toulouse, France) for stimulating discussion.

Notes and references

1 J. F. Berry, *Struct. Bonding*, 2010, **136**, 1–28.
2 J. F. Berry, in *Multiple Bonds Between Metal Atoms*, ed. F. A. Cotton, C. A. Murillo and R. A. Walton, Springer-Verlag, Boston, 2005, pp. 669–706.
3 S.-A. Hua, M.-C. Cheng, C.-h. Chen and S.-M. Peng, *Eur. J. Inorg. Chem.*, 2015, **2015**, 2510–2523.
4 S.-A. Hua, Y.-C. Tsai and S.-M. Peng, *J. Chin. Chem. Soc.*, 2014, **61**, 9–26.
5 J. A. Chipman and J. F. Berry, *Chem. Rev.*, 2020, **120**, 2409–2447.
6 I. P.-C. Liu, W.-Z. Wang and S.-M. Peng, *Chem. Commun.*, 2009, 4323–4331.
7 C.-Y. Yeh, C.-C. Wang, C.-h. Chen and S.-M. Peng, in *Redox Systems Under Nano-Space Control*, ed. T. Hirao, Springer-Verlag, Berlin Heidelberg, 2006, pp. 85–117.
8 Y. Tanaka, M. Kiguchi and M. Akita, *Chem. – Eur. J.*, 2017, **23**, 4741–4749.
9 P.-J. Chen, M. Sigrist, E.-C. Horng, G.-M. Lin, G.-H. Lee, C.-h. Chen and S.-M. Peng, *Chem. Commun.*, 2017, **53**, 4673–4676.
10 T.-C. Ting, L.-Y. Hsu, M.-J. Huang, E.-C. Horng, H.-C. Lu, C.-H. Hsu, C.-H. Jiang, B.-Y. Jin, S.-M. Peng and C.-h. Chen, *Angew. Chem., Int. Ed.*, 2015, **54**, 15734–15738.
11 V. P. Georgiev, P. J. Mohan, D. DeBrincat and J. E. McGrady, *Coord. Chem. Rev.*, 2013, **257**, 290–298.
12 A. Cornia, L. Rigamonti, S. Boccedi, R. Clérac, M. Rouzières and L. Sorace, *Chem. Commun.*, 2014, **50**, 15191–15194.
13 A. Cornia, A.-L. Barra, V. Bulicanu, R. Clérac, M. Cortijo, E. A. Hillard, R. Galavotti, A. Lunghi, A. Nicolini, M. Rouzières, L. Sorace and F. Totti, *Inorg. Chem.*, 2020, **59**, 1763–1777.
14 J. H. Christian, D. W. Brogden, J. K. Bindra, J. S. Kinyon, J. van Tol, J. Wang, J. F. Berry and N. S. Dalal, *Inorg. Chem.*, 2016, **55**, 6376–6383.
15 D. W. Brogden and J. F. Berry, *Comments Inorg. Chem.*, 2016, **36**, 17–37.
16 D. Gatteschi, R. Sessoli and J. Villain, *Molecular Nanomagnets*, Oxford University Press, New York, 2006.
17 *Molecular Nanomagnets and Related Phenomena – Struct. and Bonding Series*, ed. S. Gao, Springer-Verlag, Berlin Heidelberg, 2015, vol. 164.
18 K. Katoh, T. Komeda and M. Yamashita, *Chem. Rec.*, 2016, **16**, 987–1016.
19 E. Moreno-Pineda, C. Godfrin, F. Balestro, W. Wernsdorfer and M. Ruben, *Chem. Soc. Rev.*, 2018, **47**, 501–513.
20 A. Cornia and P. Seneor, *Nat. Mater.*, 2017, **16**, 505–506.
21 A. Gaita-Ariño, F. Luis, S. Hill and E. Coronado, *Nat. Chem.*, 2019, **11**, 301–309.

22 M. Mannini, F. Pineider, C. Danieli, F. Totti, L. Sorace, P. Sainctavit, M.-A. Arrio, E. Otero, L. Joly, J. C. Cezar, A. Cornia and R. Sessoli, *Nature*, 2010, **468**, 417–421.
23 L. Malavolti, V. Lanzilotto, S. Ninova, L. Poggini, I. Cimatti, B. Cortigiani, L. Margheriti, D. Chiappe, E. Otero, P. Sainctavit, F. Totti, A. Cornia, M. Mannini and R. Sessoli, *Nano Lett.*, 2015, **15**, 535–541.
24 C. Wäckerlin, F. Donati, A. Singha, R. Baltic, S. Rusponi, K. Diller, F. Patthey, M. Pivetta, Y. Lan, S. Klyatskaya, M. Ruben, H. Brune and J. Dreiser, *Adv. Mater.*, 2016, **28**, 5195–5199.
25 F.-S. Guo, B. M. Day, Y.-C. Chen, M.-L. Tong, A. Mansikkamäki and R. A. Layfield, *Science*, 2018, **362**, 1400–1403.
26 F.-S. Guo, B. M. Day, Y.-C. Chen, M.-L. Tong, A. Mansikkamäki and R. A. Layfield, *Angew. Chem., Int. Ed.*, 2017, **56**, 11445–11449.
27 C. A. P. Goodwin, F. Ortu, D. Reta, N. F. Chilton and D. P. Mills, *Nature*, 2017, **548**, 439–442.
28 R. Hernández Sánchez and T. A. Betley, *J. Am. Chem. Soc.*, 2015, **137**, 13949–13956.
29 D. L. Miller, R. B. Siedschlag, L. J. Clouston, V. G. Young, Y.-S. Chen, E. Bill, L. Gagliardi and C. C. Lu, *Inorg. Chem.*, 2016, **55**, 9725–9735.
30 G. A. Craig and M. Murrie, *Chem. Soc. Rev.*, 2015, **44**, 2135–2147.
31 P. Szarek, W. Wegner and W. Grochala, *J. Mol. Model.*, 2016, **22**, 63.
32 M. Nippe and J. F. Berry, *J. Am. Chem. Soc.*, 2007, **129**, 12684–12685.
33 M. Nippe, J. Wang, E. Bill, H. Hope, N. S. Dalal and J. F. Berry, *J. Am. Chem. Soc.*, 2010, **132**, 14261–14272.
34 M. Nippe, E. Bill and J. F. Berry, *Inorg. Chem.*, 2011, **50**, 7650–7661.
35 M. Nippe, Y. Turov and J. F. Berry, *Inorg. Chem.*, 2011, **50**, 10592–10599.
36 Y. Turov and J. F. Berry, *Dalton Trans.*, 2012, **41**, 8153–8161.
37 Y.-C. Liu, S.-A. Hua, M.-C. Cheng, L.-C. Yu, S. Demeshko, S. Dechert, F. Meyer, G.-H. Lee, M.-H. Chiang and S.-M. Peng, *Chem. – Eur. J.*, 2018, **24**, 11649–11666.
38 M.-C. Cheng, S.-A. Hua, Q. Lv, M. Sigrist, G.-H. Lee, Y.-C. Liu, M.-H. Chiang and S.-M. Peng, *Dalton Trans.*, 2018, **47**, 1422–1434.
39 W.-C. Chang, C.-W. Chang, M. Sigrist, S.-A. Hua, T.-J. Liu, G.-H. Lee, B.-Y. Jin, C.-h. Chen and S.-M. Peng, *Chem. Commun.*, 2017, **53**, 8886–8889.
40 F. A. Cotton, C. A. Murillo and X. Wang, *Inorg. Chem. Commun.*, 1998, **1**, 281–283.
41 A. Nicolini, R. Galavotti, A.-L. Barra, M. Borsari, M. Caleffi, G. Luo, G. Novitchi, K. Park, A. Ranieri, L. Rigamonti, F. Roncaglia, C. Train and A. Cornia, *Inorg. Chem.*, 2018, **57**, 5438–5448.
42 G. L. Guillet, K. Y. Arpin, A. M. Boltin, J. B. Gordon, J. A. Rave and P. C. Hillesheim, *Inorg. Chem.*, 2020, **59**, 11238–11243.
43 A. B. C. Simas, V. L. P. Pereira, C. B. J. Barreto, D. L. de Sales and L. L. de Carvalho, *Quim. Nova*, 2009, **32**, 2473–2475.
44 W. L. F. Armarego, *Purification of Laboratory Chemicals*, Butterworth-Heinemann, Oxford, 8th edn, 2017.
45 H. Zhao, R. Clérac, J.-S. Sun, X. Ouyang, J. M. Clemente-Juan, C. J. Gomez-Garcia, E. Coronado and K. R. Dunbar, *J. Solid State Chem.*, 2001, **159**, 281–292.
46 Q. Zhao and T. A. Betley, *Angew. Chem., Int. Ed.*, 2011, **50**, 709–712.
47 A. Klose, E. Solari, C. Floriani, A. Chiesi-Villa, C. Rizzoli and N. Re, *J. Am. Chem. Soc.*, 1994, **116**, 9123–9135.
48 A. Dirvanauskas, R. Galavotti, A. Lunghi, A. Nicolini, F. Roncaglia, F. Totti and A. Cornia, *Dalton Trans.*, 2018, **47**, 585–595.
49 Bruker, *TopSpin 4.0.6*, Bruker AXS Inc., Madison, Wisconsin, USA, 2018.
50 E. Alberico, P. Sponholz, C. Cordes, M. Nielsen, H. J. Drexler, W. Baumann, H. Junge and M. Beller, *Angew. Chem., Int. Ed.*, 2013, **52**, 14162–14166.
51 G. Mund, D. Vidovic, R. J. Batchelor, J. F. Britten, R. D. Sharma, C. H. W. Jones and D. B. Leznoff, *Chem. – Eur. J.*, 2003, **9**, 4757–4763.
52 Bruker, APEX2, SADABS, SAINT, Bruker, AXS Inc., Madison, Wisconsin, USA, 2012.
53 A. Altomare, G. Cascarano, C. Giacovazzo and A. Guagliardi, *J. Appl. Crystallogr.*, 1993, **26**, 343–350.
54 G. M. Sheldrick, *Acta Crystallogr., Sect. C: Struct. Chem.*, 2015, **71**, 3–8.
55 L. J. Farrugia, *J. Appl. Crystallogr.*, 2012, **45**, 849–854.
56 A. B. Meneses, S. Antonello, M. C. Arévalo and F. Maran, *Electroanalysis*, 2006, **18**, 363–370.
57 S. Antonello, G. Arrigoni, T. Dainese, M. De Nardi, G. Parisio, L. Perotti, A. René, A. Venzo and F. Maran, *ACS Nano*, 2014, **8**, 2788–2795.
58 R. S. Nicholson, *Anal. Chem.*, 1965, **37**, 1351–1355.
59 G. A. Bain and J. F. Berry, *J. Chem. Educ.*, 2008, **85**, 532–536.
60 I. Prisecaru, *WMOSS4 Mössbauer Spectral Analysis Software*, http://www.wmoss.org, 2009–2016.
61 J. E. Dennis, D. M. Gay and R. E. Walsh, *ACM Trans. Math. Software*, 1981, **7**, 348–368.
62 H. Adamsky, (with contributions from P. E. Hoggard, M. Atanasov, K. Eifert), *AOMX*, http://www.aomx.de/docs/html/aomxeh.html (accessed May 2020).
63 A. Bencini, C. Benelli and D. Gatteschi, *Coord. Chem. Rev.*, 1984, **60**, 131–169.
64 R. Forgan, P. Tasker and F. White, *CCDC* 1408270, 2015, DOI: 10.5517/cc1j8f29.
65 B. F. Little and G. J. Long, *Inorg. Chem.*, 1978, **17**, 3401–3413.
66 M. Gerloch, R. F. McMeeking and A. M. White, *J. Chem. Soc., Dalton Trans.*, 1975, 2452–2459.
67 A. B. P. Lever, *Inorganic Electronic Spectroscopy*, Elsevier, Amsterdam, 2nd edn, 1984.
68 F. Neese, *Wiley Interdiscip. Rev.: Comput. Mol. Sci.*, 2018, **8**, e1327.
69 R. Maurice, R. Bastardis, C. de Graaf, N. Suaud, T. Mallah and N. Guihéry, *J. Chem. Theory Comput.*, 2009, **5**, 2977–2984.

70 Y. Guo, K. Sivalingam, E. F. Valeev and F. Neese, *J. Chem. Phys.*, 2016, **144**, 094111.
71 C. Angeli, R. Cimiraglia, S. Evangelisti, T. Leininger and J.-P. Malrieu, *J. Chem. Phys.*, 2001, **114**, 10252–10264.
72 C. Angeli, R. Cimiraglia and J.-P. Malrieu, *Chem. Phys. Lett.*, 2001, **350**, 297–305.
73 F. Neese, *J. Chem. Phys.*, 2005, **122**, 034107.
74 F. Weigend and R. Ahlrichs, *Phys. Chem. Chem. Phys.*, 2005, **7**, 3297–3305.
75 F. Weigend, *J. Comput. Chem.*, 2008, **29**, 167–175.
76 S. K. Singh and G. Rajaraman, *Nat. Commun.*, 2016, **7**, 10669.
77 N. F. Chilton, R. P. Anderson, L. D. Turner, A. Soncini and K. S. Murray, *J. Comput. Chem.*, 2013, **34**, 1164–1175.
78 M. Edén and M. H. Levitt, *J. Magn. Reson.*, 1998, **132**, 220–239.
79 *ZHEEV LAPACK Driver Routine (version 2.0)*, Univ. of Tennessee, Univ. of California Berkeley, NAG Ltd., Courant Institute, Argonne National Lab, and Rice University, 1994.
80 J. Sundberg, M. S. Vad, J. E. McGrady, P. M. Björemark, M. Håkansson and C. J. McKenzie, *J. Organomet. Chem.*, 2015, **786**, 40–47.
81 R. B. Cole and J. Zhu, *Rapid Commun. Mass Spectrom.*, 1999, **13**, 607–611.
82 J. Zhu and R. B. Cole, *J. Am. Soc. Mass Spectrom.*, 2000, **11**, 932–941.
83 R. Clérac, F. A. Cotton, L. M. Daniels, K. R. Dunbar, C. A. Murillo and X. Wang, *J. Chem. Soc., Dalton Trans.*, 2001, 386–391.
84 J. F. Berry, F. A. Cotton, T. Lu, C. A. Murillo, B. K. Roberts and X. Wang, *J. Am. Chem. Soc.*, 2004, **126**, 7082–7096.
85 R. Clérac, F. A. Cotton, L. M. Daniels, K. R. Dunbar, K. Kirschbaum, C. A. Murillo, A. A. Pinkerton, A. J. Schultz and X. Wang, *J. Am. Chem. Soc.*, 2000, **122**, 6226–6236.
86 J. F. Berry, F. A. Cotton, P. Lei and C. A. Murillo, *Inorg. Chem.*, 2003, **42**, 377–382.
87 L.-P. Wu, P. Field, T. Morrissey, C. Murphy, P. Nagle, B. Hathaway, C. Simmons and P. Thornton, *J. Chem. Soc., Dalton Trans.*, 1990, 3835–3840.
88 L. C. H. Maddock, I. Borilovic, J. McIntyre, A. R. Kennedy, G. Aromí and E. Hevia, *Dalton Trans.*, 2017, **46**, 6683–6691.
89 C.-C. Wang, W.-C. Lo, C.-C. Chou, G.-H. Lee, J.-M. Chen and S.-M. Peng, *Inorg. Chem.*, 1998, **37**, 4059–4065.
90 F. A. Cotton, L. M. Daniels, C. A. Murillo and X. Wang, *Chem. Commun.*, 1999, **5**, 2461–2462.
91 F. A. Cotton, L. M. Daniels, T. Lu, A. Murillo and X. Wang, *J. Chem. Soc., Dalton Trans.*, 1999, 517–518.
92 C.-Y. Yeh, C.-H. Chou, K.-C. Pan, C.-C. Wang, G.-H. Lee, Y. O. Su and S.-M. Peng, *J. Chem. Soc., Dalton Trans.*, 2002, 2670–2677.
93 C. Yin, G.-C. Huang, C.-K. Kuo, M.-D. Fu, H.-C. Lu, J.-H. Ke, K.-N. Shih, Y.-L. Huang, G.-H. Lee, C.-Y. Yeh, C.-h. Chen and S.-M. Peng, *J. Am. Chem. Soc.*, 2008, **130**, 10090–10092.
94 R. Clérac, F. A. Cotton, K. R. Dunbar, C. A. Murillo, I. Pascual and X. Wang, *Inorg. Chem.*, 1999, **38**, 2655–2657.
95 J. F. Berry, F. A. Cotton and C. A. Murillo, *Dalton Trans.*, 2003, 3015–3021.
96 C.-K. Kuo, I. P.-C. Liu, C.-Y. Yeh, C.-H. Chou, T.-B. Tsao, G.-H. Lee and S.-M. Peng, *Chem. – Eur. J.*, 2007, **13**, 1442–1451.
97 Q. Zhao, T. D. Harris and T. A. Betley, *J. Am. Chem. Soc.*, 2011, **133**, 8293–8306.
98 D. E. Richardson and H. Taube, *Inorg. Chem.*, 1981, **20**, 1278–1285.
99 S. Santi, A. Bisello, R. Cardena and A. Donoli, *Dalton Trans.*, 2015, **44**, 5234–5257.
100 A. Ludi, in *Mixed-Valence Compounds: Theory and Applications in Chemistry, Physics, Geology, and Biology*, ed. D. B. Brown, D. Reidel Publishing Company, Dordrecht, 1980, pp. 25–47.
101 C. N. Brodsky, R. G. Hadt, D. Hayes, B. J. Reinhart, N. Li, L. X. Chen and D. G. Nocera, *Proc. Natl. Acad. Sci. U. S. A.*, 2017, **114**, 3855–3860.
102 P. Gütlich, B. Eckhard and A. X. Trautwein, *Mössbauer Spectroscopy and Transition Metal Chemistry: Fundamentals and Applications*, Springer-Verlag, Berlin Heidelberg, 2011.
103 S. J. Tereniak, R. K. Carlson, L. J. Clouston, V. G. Young, E. Bill, R. Maurice, Y.-S. Chen, H. J. Kim, L. Gagliardi and C. C. Lu, *J. Am. Chem. Soc.*, 2014, **136**, 1842–1855.
104 D. E. Freedman, W. H. Harman, T. D. Harris, G. J. Long, C. J. Chang and J. R. Long, *J. Am. Chem. Soc.*, 2010, **132**, 1224–1225.
105 W. H. Harman, T. D. Harris, D. E. Freedman, H. Fong, A. Chang, J. D. Rinehart, A. Ozarowski, M. T. Sougrati, F. Grandjean, G. J. Long, J. R. Long and C. J. Chang, *J. Am. Chem. Soc.*, 2010, **132**, 18115–18126.
106 M. Atanasov, D. Ganyushin, D. A. Pantazis, K. Sivalingam and F. Neese, *Inorg. Chem.*, 2011, **50**, 7460–7477.
107 J. Bartolomé, G. Filoti, V. Kuncser, G. Schinteie, V. Mereacre, C. E. Anson, A. K. Powell, D. Prodius and C. Turta, *Phys. Rev. B: Condens. Matter Mater. Phys.*, 2009, **80**, 014430.
108 S. K. Langley, L. Ungur, N. F. Chilton, B. Moubaraki, L. F. Chibotaru and K. S. Murray, *Chem. – Eur. J.*, 2011, **17**, 9209–9218.
109 D. Gatteschi and R. Sessoli, *Angew. Chem., Int. Ed.*, 2003, **42**, 268–297.
110 K. S. Cole and R. H. Cole, *J. Chem. Phys.*, 1941, **9**, 341–351.
111 C. Dekker, A. F. M. Arts, H. W. de Wijn, A. J. van Duyneveldt and J. A. Mydosh, *Phys. Rev. B: Condens. Matter Mater. Phys.*, 1989, **40**, 11243–11251.
112 S. M. Greer, K. M. Gramigna, C. M. Thomas, S. A. Stoian and S. Hill, *Inorg. Chem.*, 2020, **59**, 18141–18155.
113 *Molecular Magnetism: From Molecular Assemblies to the Devices*, ed. E. Coronado, P. Delhaès, D. Gatteschi and J. S. Miller, Springer Netherlands, Dordrecht, 1996.
114 A. I. Gaudette, I.-R. Jeon, J. S. Anderson, F. Grandjean, G. J. Long and T. D. Harris, *J. Am. Chem. Soc.*, 2015, **137**, 12617–12626.